Ground-Based Multifrequency Microwave Radiometry for Rainfall Remote Sensing

Frank Silvio Marzano, *Member, IEEE*, Ermanno Fionda, Piero Ciotti, *Member, IEEE*, and Antonio Martellucci

***Abstract*—Inversion algorithms for ground-based microwave radiometric retrieval of surface rain-rate, integrated cloud parameters, and slant-path attenuation are proposed and tested. The estimation methods are trained by numerical simulations of a radiative transfer model applied to microphysically-consistent precipitating cloud structures, representative of stratiform and convective rainy clouds. The discrete-ordinate method is used to solve the radiative transfer equation for plane-parallel seven-layer structures, including liquid, melted, and ice spherical hydrometeors. Besides ordinary multiple regression, a variance-constrained regression algorithm is developed and applied to synthetic data in order to evaluate its robustness to noise and its potentiality. Selection of optimal frequency sets and polynomial retrieval algorithms for rainfall parameters is carried out and discussed. Ground-based radiometric measurements at 13.0, 23.8, and 31.7 GHz are used for experimentally testing the retrieval algorithms. Comparison with rain-gauge data and rain path-attenuation measurements, derived from the three ITALSAT satellite beacons at 18.7, 39.6, and 49.5 GHz acquired at Pomezia (Rome, Italy), are performed for two selected cases of moderate and intense rainfall during 1998. Results show a fairly good agreement between retrieved and measured rainfall parameters, pointing out possible effects of nonhomogeneous beam filling at low frequencies when observing small convective cells.**

***Index Terms*—Atmospheric remote sensing, ground-based microwave radiometry, precipitation retrieval, radiative transfer modeling.**

I. Introduction

THEORETICAL and experimental results, obtained in the last few decades, have established microwave radiometry as an essential technique for retrieving atmospheric parameters in all weather conditions [1]. Ground-based microwave radiometry has been widely and successfully applied to the estimate of tropospheric temperature profiles, integrated water vapor and cloud-liquid water contents [2]–[6]. These applications have been mainly circumscribed on rain-free conditions due to the complication of separating rain effects from other atmospheric parameters [7], [8].

Manuscript received December 21, 2000; revised January 31, 2002. This work was supported in part by the Italian Space Agency (ASI), by the Italian National Research Council (CNR) through GNDCI project, and by the Italian Ministry of Scientific and Technologic Research (MURST).

F. S. Marzano and P. Ciotti are with the Dipartimento di Ingegneria Elettrica, Centro di Eccellenza CETEMPS, Università dell'Aquila, 67040 L'Aquila, Italy (e-mail: marzano@ing.univaq.it; ciotti@ing.univaq.it).

E. Fionda is with Fondazione Ugo Bordoni, Roma (Italy), 00144 Roma, Italy (e-mail: efionda@fub.it).

A. Martellucci was with Fondazione Ugo Bordoni, 00144 Rome, Italy. He is now with ESTEC—European Space Agency, NL-2200 AG Nordwijk, The Netherlands (e-mail: amartellucci@fub.it; Antonio.Martellucci@esa.int).

Publisher Item Identifier S 0196-2892(02)04601-6.

Indeed, spaceborne microwave radiometry has proved to be fairly accurate for precipitation retrieval on a global-scale, especially over ocean (e.g., [9], [10]). Considering the increasing use of multi-frequency radiometers in ground-based stations especially for communication purposes [11], [12], the question of microwave radiometry potential for retrieving rainy cloud parameters from ground is still an open issue [13], [14]. One of the major drawbacks of ground-based microwave radiometry of rainfall is represented by the impact of wetness, and possible water layers, on antenna reflectors when measuring brightness temperatures [15]–[17]. This effect can contaminate radiometric measurements in a significant way thus misleading any cloud-parameter estimate if not taken into account in the inversion algorithm.

Rain-gauge are typical instruments for measuring rainfall at ground. With respect to rain-gauges, microwave radiometers can give an estimate of integrated rainy-cloud parameters [6]–[8]. These latter products can be of some interest for assimilation and validation purposes within numerical weather forecast models. Moreover, they could be used for comparison and validation of rain contents derived from satellite microwave radiometers, especially over land where the uncertainties of spaceborne radiometric estimates are larger [18]. It should not be also disregarded the possibility to estimate slant-path rain attenuation from radiometric data with a significant benefit on satellite link-budget design at frequencies where no experimental links are available [12], [14]. Finally, notice that the exploitation of ground-based microwave radiometry might also be useful when weather radars are co-located [19], since radiometric estimates of rainfall might be used as a further constraint within the inversion schemes of radar reflectivity measurements, as already shown for airborne observations [20], [8].

Generally speaking, any inversion algorithm can be trained by using either experimental measurements or simulated data. The use of experimental measurements is limited by their scarcity or even their lack, especially in rainy clouds. The modeling approach is generally more versatile, even though it requires a thorough insight into the electromagnetic interaction between the microwave radiation and the scattering medium [21], [22]. Moreover, a modeling approach needs to produce synthetic data in agreement with available measured ones in order to yield unbiased estimates [18]. The radiative transfer theory has been the most used approach so far to account for the multiple scattering and the vertical inhomogeneity of the atmosphere in the presence of hydrometeor scattering [21]–[23].

The objective of this work is to investigate the potentiality of ground-based microwave radiometry for rainy-cloud param-

eter retrieval by optimizing frequency sets and retrieval algorithms best suited for observing both stratiform and convective precipitation. Inversion algorithms for ground-based retrieval of precipitation parameters are developed, adopting a model-based approach. Vertical profiles of stratiform and convective precipitation are generated by means of a microphysically-consistent statistical model. The discrete-ordinate method is used to solve the radiative transfer equation for plane-parallel structures, including liquid, melted, and ice spherical hydrometeors. Constrained multiple regression techniques are developed and tested on synthetic data in order to understand their potential in terms of robustness to noise together with the analysis of a frequency set best suited for rainfall estimation. Finally, ground-based radiometric measurements at 13.0, 23.8, and 31.7 GHz are used for experimentally testing the retrieval algorithms. Comparison with rain-gauge data and rain path-attenuation measurements, derived from a satellite beacon at 18.7, 39.6, and 49.5 GHz acquired at Pomezia (Rome, Italy), are performed for two selected cases of moderate and intense rainfall.

II. Rainfall Radiative Models

The scarcity of *in situ* meteorological data, concerning cloud and precipitation structures, suggests tackling the forward, and consequently the inverse problem, by using cloud and radiative models. A general theoretical framework to model the down-welling brightness temperature, measured by a microwave radiometer and due to clouds and precipitation, is given by the radiative transfer theory [21], [22]. Consider a stratified atmosphere with a bottom level at $z = 0$ (surface) and a top height at $z = H$. Let us define a vertical coordinate in terms of optical thickness τ_ν or path attenuation A_ν [dB] at frequency ν such that

$$\tau_\upsilon(z', z'') = \frac{A_\upsilon(z', z'')}{4.343} = \int_{z'}^{z''} k_{e\upsilon}(z)\, dz \tag{1}$$

where $\tau_\nu = 0$ at $z = H$ and $\tau_\nu = \tau_{\nu_s} = \tau_\nu(0, H)$ at $z = 0$ with $k_e\nu$ the extinction coefficient [km^{-1}]. It is also convenient to introduce the zenith-angle cosine $\mu = |\cos(\theta)|$ with θ the zenith angle and $0 \le \theta \le \pi/2$ so that $0 \le \mu \le 1$ for downward directions and $-1 \le \mu \le 0$ for upward directions.

For a plane-parallel geometry, the unpolarized azimuthally-symmetric down-welling brightness temperature $T_B(\tau_{\nu s}, \mu)$, observed from ground at a frequency ν, can be formally expressed by means of the integral form of *radiative transfer equation* (RTE), that is [21], [22]

$$T_B(\tau_{\upsilon s}, \mu) = T_B(0, \mu)e^{-\tau_{\upsilon s}/\mu} + \frac{1}{\mu}\int_0^{\tau_{\upsilon s}} J(\tau_\upsilon, \mu) \cdot e^{-(\tau_{\upsilon s}-\tau_\upsilon)/\mu}\, d\tau_\upsilon \tag{2}$$

where $J(\tau_\nu, \mu)$ is the pseudo-source function given by

$$J(\tau_\upsilon, \mu) = \frac{w(\tau_\upsilon)}{2}\int_{-1}^{1} p(\tau_\upsilon, \mu, \mu')T_B(\tau_\upsilon, \mu')\, d\mu' + [1 - w(\tau_\upsilon)]T(\tau_\upsilon) \tag{3}$$

with w the volumetric albedo (i.e., $w = k_{s\nu}/k_{e\nu}$ with $k_{s\nu}$ the scattering coefficient), p the volumetric azimuthally averaged scattering phase function, and T the physical temperature. The first term of J is sometimes referred to as a multiple scattering source, while the second item represents thermal emission. It is worth noting that the scattering phase function in (3) is normalized to 2 (with respect to $d\mu$) and that the boundary conditions to couple with (2) in case of absence of collimated incident radiation at $z = 0$ and a near-flat bottom surface are

$$T_B(0, \mu) = T_c \tag{4}$$

$$T_B(\tau_{\upsilon s}, -\mu) = (1 - e_s)T_B(\tau_{\upsilon s}, \mu) + e_s T_s \tag{5}$$

where $T_c = 2.73$ K is the cosmic background brightness temperature, $T_B(\tau_{\nu s}, -\mu)$ is the upwelling T_B at the surface, while e_s and T_s are the surface emissivity and physical temperature, respectively [24]. If the atmosphere is horizontally stratified, continuity equations of brightness temperatures at intermediate boundaries are also requested to solve the integral equation [21].

From (2) and (3), it is apparent that, in case of scattering atmosphere, solutions for $T_B(\tau_{\nu s}, \mu)$ in a closed form can be derived only under given approximations. For instance, if $w = 0$ in (3), expression (2) becomes the RTE analytical solution for clear-air applications [25]. In order to solve (2) in the general case, a numerical technique can be used as an alternative.

The discrete-ordinate method, as exposed in [26], has been chosen to numerically solve RTE in this paper. The atmosphere is assumed to consist of L adjacent homogeneous layers in which volumetric albedo w, extinction coefficient $k_{e\nu}$ and phase function p are taken to be constant within each layer. Physical temperature is supposed to be linearly dependent on the vertical coordinate within each layer. The angular variation in μ is discretized into $2N_\mu$ points so that the multiple scattering in (3) is transformed into a sum by means of a Gaussian quadrature (which implicitly ensures the normalization of the phase function).

Once set up the radiative transfer scheme, a model of rainy clouds in terms of vertical structures of hydrometeor content distribution and associated single-scattering parameters (i.e., w, $k_{e\nu}$ and p) is needed. Meteorological environment in terms of pressure, temperature and humidity profiles should be specified as well in order to describe gaseous absorption. The next two sections will be devoted to these aspects.

A. Rainfall Models

In previous works, we described a technique to use cloud-resolving model outputs to physically constrain the vertical correlation of hydrometeor contents within cloud layers [9], [10], [18]. Numerical outputs of a three-dimensional time-dependent cloud mesoscale model have been used for generating cloud-structure data set, explicitly describing the gross vertical distribution of four species of hydrometeors: cloud droplets, raindrops, graupel particles, and snow particles [9], [10]. Cloud structures have been vertically resolved in seven homogeneous layers with a variable vertical resolution of about 1.5 km.

A classification of cloud structures into meteorological cloud genera has been applied in order to derive both mean vertical profiles and covariance matrices of hydrometeor contents of each cloud class [27], [18]. By using seasonal statistical values of meteorological profiles, mean structures of cloud genera have

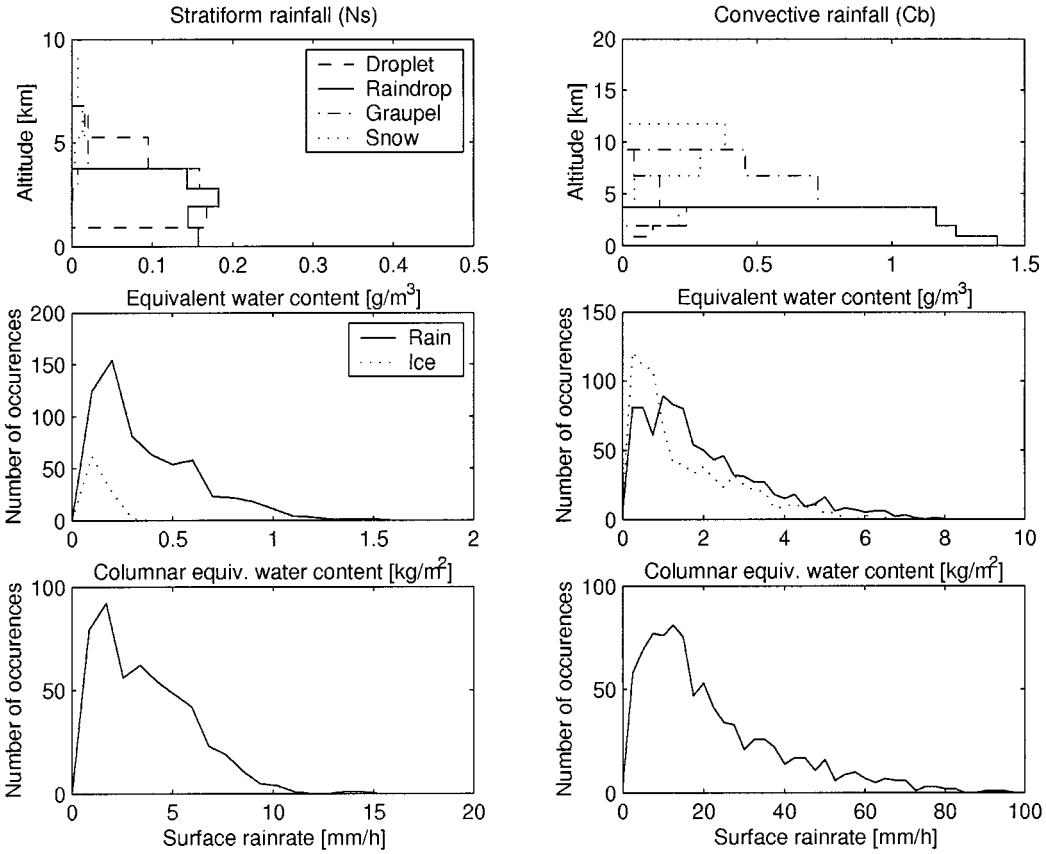

Fig. 1. Stratiform rainfall (Ns) and convective rainfall (Cb) characteristics shown in left and right panels, respectively. Top panels: average vertical profiles of EWCs for each hydrometeor species, i.e., cloud, rain, graupel, and snow, derived from the statistically-generated rainfall cloud data set. Middle panels: histogram of columnar EWCs of rain and ice hydrometeors. Bottom panels: histogram of surface rain rates.

been tuned to Mediterranean area conditions. The freezing level has been chosen as a driving parameter for hydrometeor content scaling with the constraint to have an invariant *equivalent water content* (EWC) of each hydrometeor integrated within any scaled layer. Radio-sounding data, acquired at Pratica di Mare station (Rome, Italy), have been used for thermal and humidity characterization of modeled meteorological environment. It is opportune to point out that the radio-sounding station is few kilometers far from the experimental site, illustrated in Section IV.

The classified cloud data set has been then extended by means of a Monte Carlo statistical procedure, based on the use of a truncated Gaussian multivariate generator defined by mean and covariance matrix of the hydrometeor contents of each class [18]. Meteorological variables have been supposed to be uniformly variable around their mean values within a given percentage. In this work we have considered both stratiform rainfall (i.e., nimbostratus, stratus and altostratus) and convective rainfall (i.e., cumulonimbus, cumulonimbus with incus and cumulus congestus) [27]–[29]. As a result, a data set of 5000 cloud structures has been statistically generated retaining the physical and statistical features of the input microphysical cloud model.

Fig. 1 shows a typical summery average vertical structure of stratiform rainfall (Ns) and convective rainfall (Cb), characterized by the vertical distribution of four hydrometeor categories together with histograms of *columnar equivalent water content* (CEWC) of total ice (graupel plus snow) and rain and histograms of associated surface rain-rate. Stratiform rainfall shows, as expected, less amount of water and ice contents than that of convective rainfall, with a gross melting layer just below the freezing level (determined by the rain top height) [10], [29]. Convective clouds are characterized by the presence of a large amount of ice above the freezing level itself due to ice nucleation processes [27]. Surface rain-rate histograms exhibit a log-normal probability density function (PDF) shape with maxima of about 15 mm/h and 100 mm/h for Ns and Cb, respectively.

Consistently with the RTE adopted scheme, within each cloud layer the temperature has been assumed linearly dependent on the height. Microwave gaseous absorption has been computed by means of the Liebe model [30]. The land-surface emission has been characterized by a Lambertian emissivity model, depending on surface humidity [18]. The humidity value has been supposed randomly variable in order to cover a large variety of surface conditions.

The hydrometeor shapes have been assumed all spherical and characterized by inverse-exponential particle size distributions (PSD's) [18], [29]. In the logarithmic plane the intercept of a PSD has been derived from the assigned EWC within each layer, while the slope has been parameterized to surface rain-rate using a Marshall–Palmer, a Sekhon–Srivastava and a Gunn–Marshall PSD for raindrops, ice graupel and snow, respectively [18], [14]. Cloud droplets have been assumed to follow a modified Gamma PSD. Radius size ranges of cloud droplets, raindrops, ice graupel and snow have been fixed

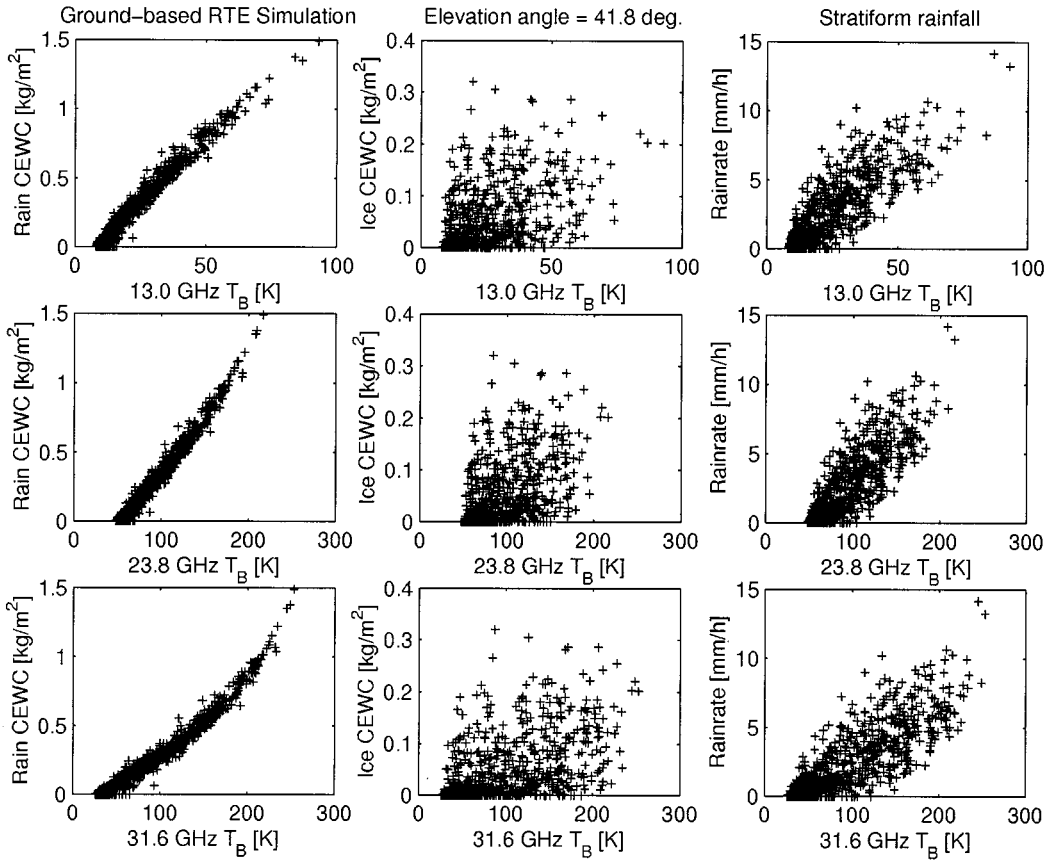

Fig. 2. For stratiform rainfall, numerical simulations of brightness temperatures (T_Bs) for a 41.8°-elevation pointing angle at 13.0 GHz (bottom panels), at 23.8 GHz (middle panels) and at 31.7 GHz (bottom panels) as a function of columnar EWCs of rain (left panels), columnar EWCs of total ice (central panels), and surface rain-rate (right panels).

to 0.001–0.01, 0.1–3, 0.1–5, and 0.1–10 mm, respectively. Density of ice graupel and snow has been set to 0.6 and 0.1 g cm^{-3}, respectively. Snow dielectric constant has been derived by a second-order Maxwell–Garnett formula for inclusions of air in an ice matrix [29]. For stratiform rain clouds a melting layer has been modeled by choosing a water-coated ice-particle model with a coating fraction of 10% [18]. Indeed, oblateness of raindrops can cause a depolarization signal, depending on cloud stage and wind circulation [31]. Even though ice crystals are not spherical, it should be noted that for ground-based rainfall observations the contribution of the iced layers the to the total brightness temperature is fairly small [21].

B. Numerical Simulations

It is worth mentioning that, due to the assumptions of a plane-parallel atmosphere and single-scattering predominance for computing the atmospheric extinction, the total path attenuation at angles away from zenith can be simply obtained by applying the "cosecant" law [12]. Moreover, this modeling framework does not allow us to take into account the horizontal inhomogeneity of precipitation, that is beam filling problem which might be relevant for convective storm clouds [13], [14].

However, in this respect it has been shown that the one-dimensional (1-D) RTE can be used to approximate three-dimensional (3-D) simulation in the frequency and rainfall ranges considered here by selecting a suitable inclined plane-parallel structure along the line-of-sight [14]. This means that, even though the internal horizontal inhomogeneity of rain clouds cannot be addressed, the above 1-D modeling framework could be easily adapted to observations of rainfall outside the rain cell.

By using the coupled rainfall and radiative transfer model illustrated before, a large data set, consisting of 5000 cloud structures together with related path attenuations and brightness temperatures at given frequencies and observation angles, has been simulated. The analysis has included the frequency bands of OLYMPUS and ITALSAT beacons, i.e., 12.5, 18.7, 29.7, 39.6, and 49.5 GHz [11], [12], and the most common channel frequencies of ground-based radiometers, that is 13.0, 20.6, 22.3, 23.8, 31.7, 36.5, 50.2, 53.8, and 90 GHz [3], [8], [12]. The observation angle has been chosen in accordance to the application, in principle between 0° and 90° elevation. Practically, we will show results only for 41.8° elevation in order to be able to compare simulations with measurements in Section IV.

For a stratiform rainfall Fig. 2 shows the rain-rate, rain and total ice CEWC's as a function of the down-welling brightness temperature at 13.0, 23.8, and 31.7 GHz with a 41.8° elevation angle. Fig. 3 shows the same of Fig. 2, but for a convective rainfall.

As expected, dynamic ranges of T_B are very much different between Ns and Cb. We note a substantial linearity for the low frequency at 13.0 GHz both for Ns and Cb, while saturation effects for high rain-rates and columnar contents at 23.8 and 31.7 GHz for a Cb. The latter effect is due to the saturation

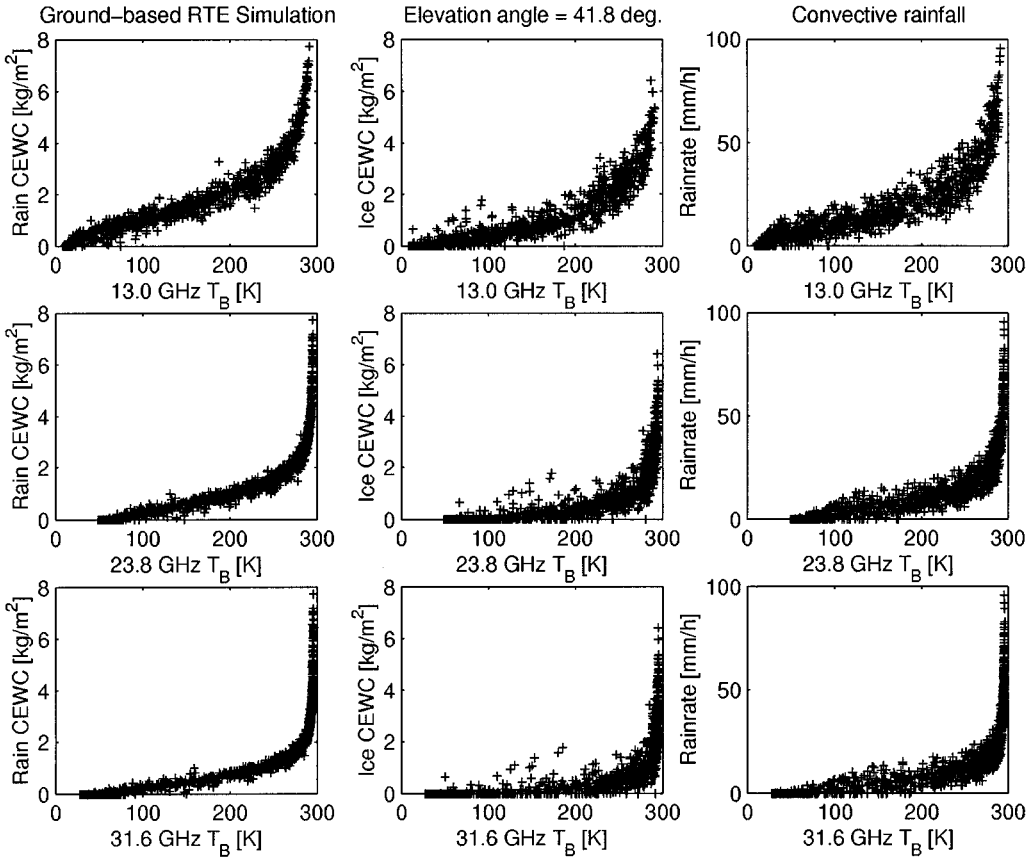

Fig. 3. The same as in Fig. 2, but for a convective rainfall.

of atmospheric opacity (shown later) when a mature convective cloud structure is radiometrically observed from ground. The higher dispersion of rain-rate plots has a physical meaning since in our modeling surface rain-rate is related to the rain content of the near-surface layer. Since T_B observations are integrated measurements along the path, it is understandable they are much more correlated with columnar parameters than surface ones. Columnar ice content is less correlated with T_B observations than rain one, as expected.

Similarly to Fig. 2, Fig. 4 shows the path attenuation for the ITALSAT channel frequencies at 18.7, 39.6, and 49.5 GHz as a function of the down-welling brightness temperature at 13.0, 23.8, and 31.7 GHz, both for a 41.8° elevation angle. While Fig. 4 refers to stratiform rainy clouds, Fig. 5 illustrates the same but for convective rainfall. Path attenuation increases with frequency and T_Bs tend to saturate for high values of attenuation at higher frequencies due to the large rainfall and graupel albedo. Up to about 250 K the 13.0-GHz channel has almost a linear response to path attenuation due to the lower atmospheric opacity.

III. Estimation of Rainfall Parameters

In the next sections nonlinear multiple regression algorithms will be illustrated for different sets of frequency channels and precipitation genera. Notice that a vectorial notation will be introduced to simplify the exposition of the retrieval techniques: uppercase bold letters will indicate matrices, while lowercase bold letters will indicate column vectors.

A. Multiple Regression Algorithms

If ρ_h is the equivalent water content (in g m^{-3}) of each hydrometeor, then the corresponding columnar equivalent water content is given by

$$C_h = \int_0^H \rho_h(z)\, dz \tag{6}$$

where the subscript $h = [c, r, g, i]$ varies for cloud droplet, raindrop, graupel, and ice-crystal hydrometeor species, respectively, and H is the top-of-the-atmosphere height. Of course, depending on the cloud genus, some hydrometeor are confined to a given altitude region, as shown in Fig. 1.

For inversion purposes, we can define a *predictand* (or *parameter*) vector $\mathbf{x}$ as the union of all the unknown random parameters to be estimated by radiometric measurements. The parameters are surface rainfall rate R [mm h^{-1}], CEWC of the four hydrometeors indicated as C_c, C_r, C_g, and C_i [kg m^{-2}] consistently with (6), and path attenuation at given (here three) frequencies indicated as $A_{\nu 1}$, $A_{\nu 2}$, and $A_{\nu 3}$ [dB] consistently with (1). Vectorially, we have eight elements for $\mathbf{x}$, that is $\mathbf{x} = [R, C_c, C_r, C_g, C_i, A_{\nu 1}, A_{\nu 2}, A_{\nu 3}]^T$.

If $\mathbf{x}$ represents the atmospheric state, a multifrequency radiometric vector $\mathbf{t}$ will indicate the simulated ground-based brightness temperatures at a given observation angle μ_o and for a set of N chosen frequencies. That is, $\mathbf{t}$ represents the observation without errors, whose elements are such that

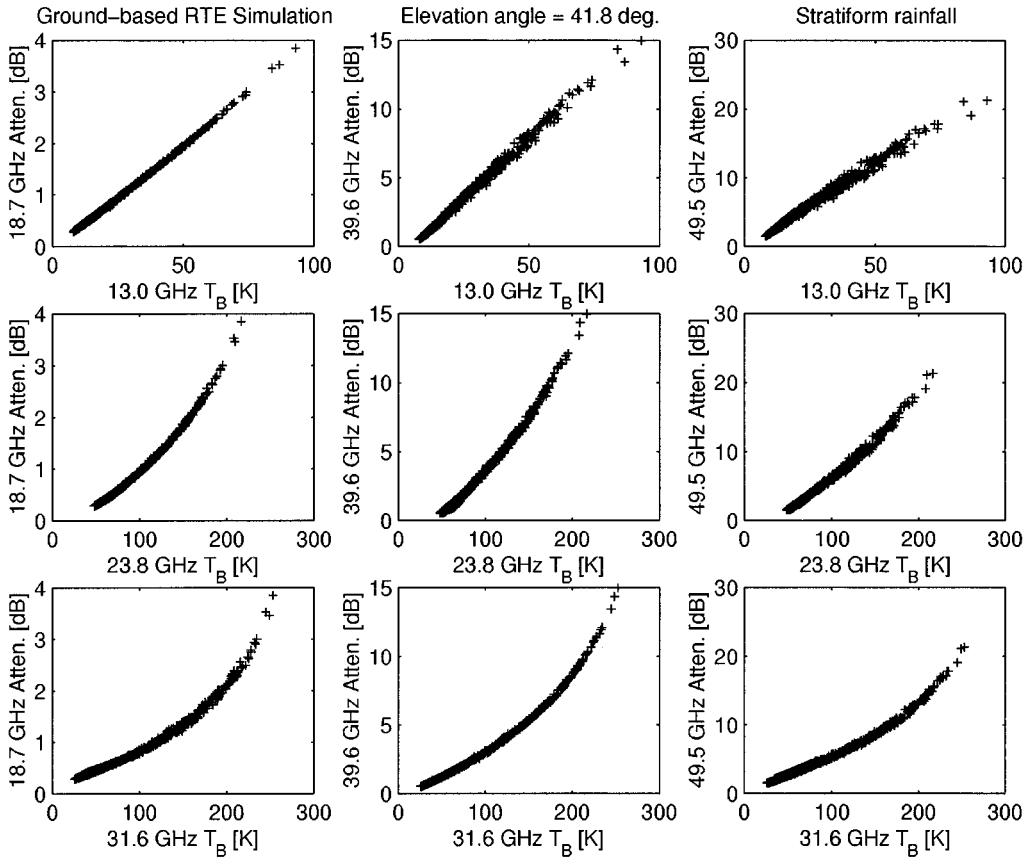

Fig. 4. For stratiform rainfall, numerical simulations of brightness temperatures (T_Bs) for a 41.8°-elevation pointing angle at 13.0 GHz (top panels), at 23.8 GHz (middle panels) and at 31.7 GHz (bottom panels) as a function of path attenuation along the same slant path at 18.7 GHz (left panels), at 39.6 GHz (central panels) and at 49.5 GHz (right panels).

$\mathbf{t} = [T_B(\tau_{\nu 1s}, \mu_o), \ldots, T_B(\tau_{\nu Ns}, \mu_o)]^T$, where the superscript T stands for matrix transposition. Examples of $\mathbf{t}$ realizations are illustrated in previous Figs. 2–5.

The vector of multi-frequency radiometric measurements (i.e., observations with errors), corresponding to $\mathbf{t}$, will be indicated by $\mathbf{t}_m$. The vector $\mathbf{t}_m = [T_{Bm}(\tau_{\nu 1s}, \mu_o), \ldots, T_{Bm}(\tau_{\nu Ns}, \mu_o)]^T$ is called the *predictor* (or *measurement*) vector. The relationship between $\mathbf{t}$ and $\mathbf{t}_m$ is modeled through a random noise vector, superimposed to simulation outputs $\mathbf{t}$. This noise is supposed here to be an additive Gaussian variable ε_t such that

$$\mathbf{t}_m = \mathbf{t} + \varepsilon_t \tag{7}$$

where uncorrelation among each radiometric channel is assumed. It is worth mentioning that ε_t summarizes not only the instrumental noise (which is generally known in terms of measurement accuracy), but also the model and measurement unknowns.

A model-based approach to discrete inversion would need an explicit forward model to derive a physical retrieval scheme [2], [32]. In our case, the forward model should relate a given atmospheric state $\mathbf{x}$, characterized by clouds and rainfall, to a set of multi-frequency radiometric measurements $\mathbf{t}_m$, formally as follows:

$$\mathbf{t}_m = \mathbf{F}(\mathbf{x}). \tag{8}$$

In (8), $\mathbf{F}$ is the matrix radiative-transfer forward model, which is highly non linear in the considered case as implicitly expressed by (2) and (3).

The deduction of $\mathbf{F}$ is not an easy task within rainfall remote sensing. A way to overcome this problem is to adopt a regression approach and trying to linearized the inverse operator (i.e., $\mathbf{F}^{-1}$) between $\mathbf{x}$ and $\mathbf{t}_m$ [32]. We refer to vector values of $\mathbf{x}$ and $\mathbf{t}_m$ centered around their respective reference (e.g., mean) values $\mathbf{m}_x$ and $\mathbf{m}_t$, i.e.,

$$\begin{aligned} \mathbf{x}_c &= \mathbf{x} - \mathbf{m}_x \\ \mathbf{t}_{mc} &= \mathbf{t}_m - \mathbf{m}_t. \end{aligned} \tag{9}$$

If a linear relation is assumed between the centered measurement vector $\mathbf{t}_{mc}$ and the parameter vector $\mathbf{x}_c$, then the *ordinary multiple regression* (OMR) estimation of $\mathbf{x}_c$ is given by [32], [33]

$$\hat{\mathbf{x}}_c = \mathbf{D}_{\mathrm{OMR}}\mathbf{t}_{mc} = \mathbf{S}_{xt}\mathbf{S}_t^{-1}\mathbf{t}_{mc} \tag{10}$$

where $\mathbf{D}_{\mathrm{OMR}}$ is the OMR coefficient matrix, $\mathbf{S}_{xt}$ and $\mathbf{S}_t$ are the cross-covariance between $\mathbf{x}_c$ and $\mathbf{t}_{mc}$ and the auto-covariance of $\mathbf{t}_{mc}$, respectively. Note that (10) is also called ordinary least-square solution or D-matrix technique.

Apart from its implementation simplicity, another relevant feature of (10) is that, if the relationship between $\mathbf{x}_c$ and $\mathbf{t}_{mc}$ is not linear, but it can be expanded into a Taylor's series, then

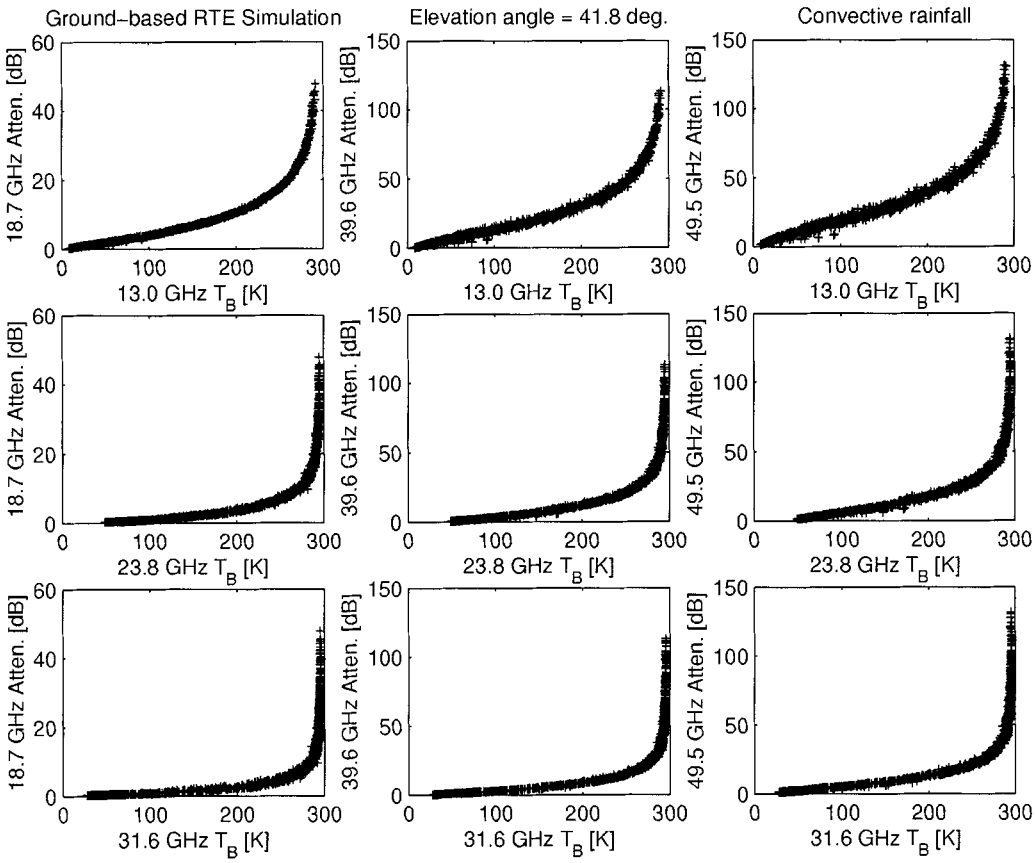

Fig. 5. The same as in Fig. 4, but for a convective rainfall.

a nonlinear estimation of $\mathbf{x}_c$ can still be performed [32]. Moreover, $\mathbf{t}_{mc}$ and $\mathbf{x}_c$ can represent any function of the desired parameter and measurement vectors.

A further appealing aspect of (10) is that it can be deduced even under particular constraints in order to ensure more robustness to test data noise. This aspect is very suitable to the scenario we need to face when retrieving rainfall by means of microwave remote sensors and a model-based approach. The random error vector ε_t, generally characterized by a systematic and a random component, should take into account in (7) modeling as well as measurement noise. For instance, our forward model is formulated for unpolarized T_Bs so that depolarization effects due to particle shapes are not reproduced. In this regard, there is an evidence for discrepancies up to 10 K attributed to polarization difference [31]. Moreover, plane-parallel assumption and gross vertical discretization can be insufficient to characterize a highly variable and inhomogeneous cloud structures. Numerical simulations have shown a relevant impact of ice vertical resolution on upwelling T_Bs, even though not as much for a down-welling radiation case (say less than 5 K at Ka band) [9]. Finally, the impact of water layers on the antenna surface can lead to a bias of rainfall signals with polarization-dependent values for moderate-to-intense rainfall rates up to 50 K [16].

It is clear that any estimator of rainfall parameters should be devised with a special robustness with respect to these uncertainties. Extending an approach proposed in literature [33], it is possible to give a robust estimation of $\mathbf{x}_c$, based on a *variance-constrained multiple regression* (VMR) method whose formulation is given by

$$\hat{\mathbf{x}}_c = \mathbf{D}_{\mathrm{VMR}}\mathbf{t}_{mc} = \mathbf{S}_{xt}(\mathbf{S}_t + \gamma\mathbf{S}_v)^{-1}\mathbf{t}_{mc} \tag{11}$$

where $\mathbf{D}_{\mathrm{VMR}}$ is the VMR coefficient matrix, γ is the *constraint factor*, and $\mathbf{S}_v$ is a diagonal matrix derived from the auto-covariance matrix $\mathbf{S}_t$. Details on the derivation of (11) are exposed in the Appendix. Obviously, for $\gamma = 0$, (11) yields (10), while by definition $\gamma = 1$ means to double the variances of $\mathbf{S}_t$.

The critical aspect in the use of (11) is the choice of the constraint γ. Empirical ways can be followed by successive trials starting, for instance, with $\gamma = 1$ and choosing to minimize a residual error on a test set. In order to select an objective, and possibly quantitative, criterion we have imposed that the estimates from (11) must be positive defined for any $\mathbf{t}_{mc}$ belonging to the test set, starting from $\gamma = 0$ [34]. This physical condition, which basically corresponds to impose a projection onto a convex domain, can be stated as

$$\gamma\colon \hat{\mathbf{x}} = \mathbf{m}_{\mathbf{x}} + \mathbf{S}_{xt}(\mathbf{S}_t + \gamma\mathbf{S}_v)^{-1}\mathbf{t}_{mc} \geq 0 \qquad \forall\, \mathbf{t}_{mc}. \tag{12}$$

Clearly, if (10) already satisfies the condition (12), γ is set to zero.

By using (10) or (11) together with (9) in a quite general form, we can choose a polynomial expression in order to fit simulated parameters and measurements using the cloud radiative data set,

described in Section II. Assuming a cubic form as an example, the measurement vector is given by

$$\begin{aligned}\mathbf{t}_m = [&T_{Bm}(\tau_{\nu 1s}, \mu_o), \ldots, T_{Bm}(\tau_{\nu Ns}, \mu_o)\\ &T^2_{Bm}(\tau_{\nu 1s}, \mu_o), \ldots, T^2_{Bm}(\tau_{\nu Ns}, \mu_o)\\ &T^3_{Bm}(\tau_{\nu 1s}, \mu_o), \ldots, T^3_{Bm}(\tau_{\nu Ns}, \mu_o)]^T.\end{aligned}$$

Therefore, surface rainfall rate R can be directly estimated from T_B measurements by means of

$$\hat{R} = a_{00} + \sum_{k=1}^{N}[a_{1k}T_{Bm}(\nu_k) + a_{2k}T^2_{Bm}(\nu_k) + a_{3k}T^3_{Bm}(\nu_k)] \tag{13}$$

where a_{jk} are the regression coefficients with subscript k denoting the available N radiometric frequencies and $T_{Bm}(\nu_k)$ stands for $T_{Bm}(\tau_{\nu s}, \mu_o)$. Mixed terms in (13) have been neglected (see next section) and the intercept term a_{00} is related to the mean (reference) values of $\mathbf{x}$ and $\mathbf{t}$.

Similar expressions can be written for columnar hydrometeor contents C_h (with $h = c, r, g, i$ for cloud, rain, graupel, and ice hydrometeor, respectively), that is

$$\begin{aligned}\hat{C}_h = b_{h00} + \sum_{k=1}^{N}[&b_{h1k}T_{Bm}(\nu_k) + b_{h2k}T^2_{Bm}(\nu_k)\\ &+ b_{h3k}T^3_{Bm}(\nu_k)]\end{aligned} \tag{14}$$

being b_{hjk} the regression coefficients. For the total path attenuation A_ν with ν the considered channel frequency, we have

$$\hat{A}_\nu = c_{\nu 00} + \sum_{k=1}^{N}[c_{\nu 1k}T_{Bm}(\nu_k) + c_{\nu 2k}T^2_{Bm}(\nu_k) + c_{\nu 3k}T^3_{Bm}(\nu_k)] \tag{15}$$

with $c_{\nu_{jk}}$ the regression coefficients.

It is worth mentioning that, with respect to the clear-air case, regression coefficients of (13)–(15) are dependent on the observation angle, and cannot be scaled to any elevation by using the so called "cosecant" law, as done in clear-air conditions [12], [25]. Finally, this set of coefficients will be different if either OMR or VMR estimation technique is applied.

B. Frequency-Set and Algorithm Selection

For testing the retrieval algorithms illustrated above, we have used synthetic data obtained from the simulated database. The synthetic database has been subdivided in two different sets, one used for training the inversion algorithms and the other for testing them. The numerical tests have been performed on all parameters defined by (13)–(15). The main goal of this section is to answer to the following questions.

1) What is the optimal frequency set to estimate rainfall parameters for Ns and Cb cases?
2) Is cubic multiple regression the best suited form for (10) or (11)?
3) What's the benefit of using constrained multiple regression (i.e., VMR algorithm) with respect to OMR?
4) How can we perform a distinction between Ns and Cb cloud data set in the inversion step?

Before showing the results, it is opportune to introduce some vector indexes to summarize the results of the following statistical analysis. To this aim, we refer to the residual estimate error ε_x defined as

$$\varepsilon_x = \hat{\mathbf{x}} - \mathbf{x} \tag{16}$$

where $\mathbf{x}$ is the model (true) value. Consequently, as a measure of error variance we can introduce the Fractional Variance Reduction (FVR) as follows [2]:

$$\text{FVR} = \frac{\text{Tr}[\mathbf{S}_x - \mathbf{S}_{\varepsilon x}]}{\text{Tr}[\mathbf{S}_x]} \tag{17}$$

where Tr indicates matrix-trace operator and $\mathbf{S}_{\varepsilon x}$ is the auto-covariance of ε_x. Optimal value of FVR is 1, which means that estimate errors are zero or we are in the case $M = N$ (number of parameters equal to measurements) [2]. The worst case is when FVR tends to $-\infty$, indicating that error variances are much higher that training set variances.

To complement (17) in order to give a measure of error bias, the Fractional Mean Reduction (FMR) can be defined as

$$\text{FMR} = \frac{\text{Tr}[diag(\mathbf{m}_x - \mathbf{m}_{\varepsilon x})]}{\text{Tr}[diag(\mathbf{m}_x)]} \tag{18}$$

where $diag$ indicates the diagonal operator (whose output, when applied to a vector $\mathbf{a}$ of M components, is a square matrix of order M with the elements of $\mathbf{a}$ on the main diagonal), while $\mathbf{m}_x$ and $\mathbf{m}_{\varepsilon x}$ are the mean vector of $\mathbf{x}$ and ε_x, respectively. In other words $\mathbf{m}_{\varepsilon x}$ represents the error bias vector. Optimal value of FMR is 1, which means that the error bias is zero, while FMR > 1 and FMR < 1 indicate an underestimation and an overestimation, respectively, of predicted values with respect to true values.

Coming back to our objectives, Figs. 6 and 7 can be used to answer to the first point about optimal frequency sets. They show for a Ns and Cb case, respectively, FMR and FVR values for rain-rate, columnar contents, and path attenuation estimates selecting various frequency sets. Results have been obtained by using a cubic estimator as given in an explicit form in (13)–(15). Note that in this analysis we concentrate on the estimate of path attenuation at 3 frequencies corresponding to ITALSAT beacons at 18.7, 39.6, and 49.5 GHz observed at 41.8°, as already mentioned (see Figs. 4 and 5). Using other elevation angles for both T_B and A does not modify the following basic conclusions.

The considered frequency sets are nine and constructed as follows: FS1 = [13, 23, 31 GHz], FS2 = [13, 23, 50 GHz], FS3 = [13, 31, 50 GHz], FS4 = [6, 13, 31 GHz], FS5 = [13, 19, 31 GHz], FS6 = [23, 31, 53 GHz], FS7 = [13, 31 GHz], FS8 = [23, 31 GHz], FS9 = [23, 36 GHz]. The combination has been carried out by considering operational cases where three- or dual-channel microwave radiometers are available. Low frequencies have been privileged considering simulation results, while the 53-GHz channel has been introduced to consider the impact of a temperature-profile sounding channel as well. We excluded the frequency at 90 GHz, but results are not too much different than including the 50-GHz channel.

Different conclusions are drawn from looking at Figs. 6 and 7. In the case of Ns, the optimal choice tends to include high

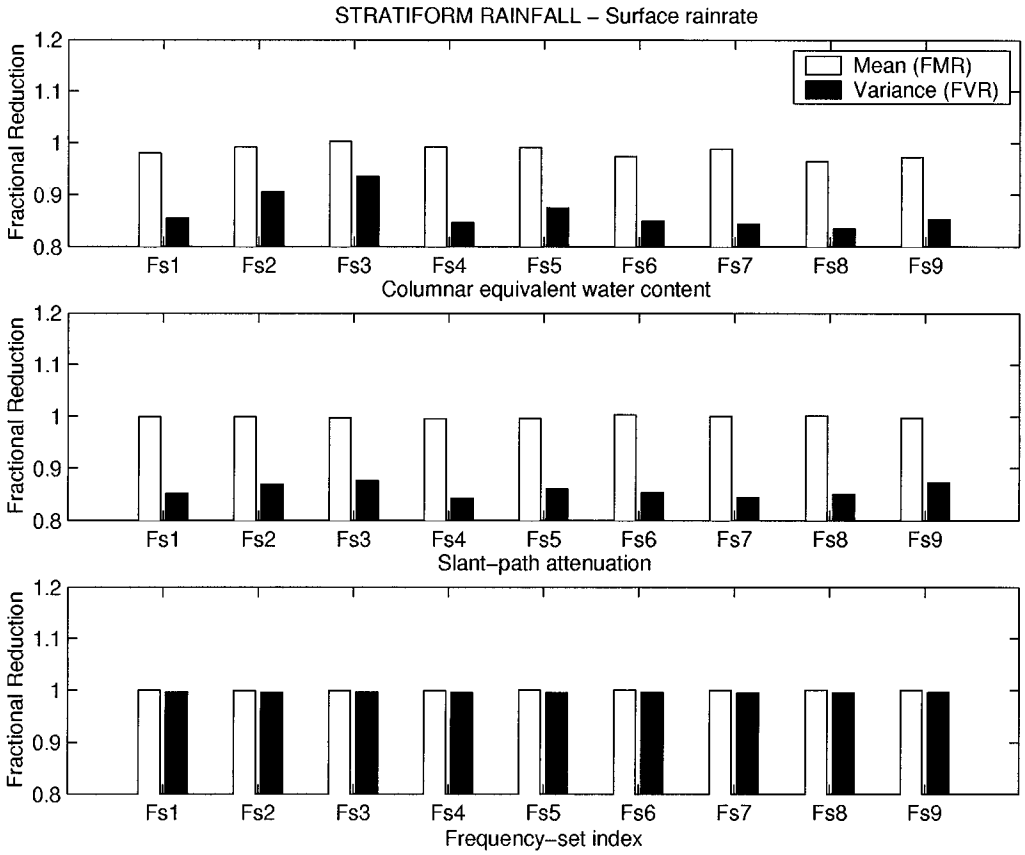

Fig. 6. For stratiform rainfall, comparison of 9 different frequency sets (Fsj with $j = 1$–9) in terms of fractional mean reduction (FMR) and fractional variance reduction (FVR) for surface rain-rate (top panels), columnar EWC's of rain (middle panels) and path attenuation at ITALSAT frequencies (bottom panels). Frequency sets in GHz are constructed as follows: Fs1 = [13, 23, 31], Fs2 = [13, 23, 50], Fs3 = [13, 31, 50], Fs4 = [6, 13, 31], Fs5 = [13, 19, 31], Fs6 = [23, 31, 53], Fs7 = [13, 31], Fs8 = [23, 31], Fs9 = [23, 36]. The test set is a subsample of what is shown in Figs. 2 and 4, while the retrieval algorithm is a cubic ordinary multiple regression (OMR).

frequencies since they show a wide dynamic range with a relevant sensitivity to rainfall parameters. In the case of Cb, high frequencies become less important because they are affected by saturation for high rain-rates, while low frequencies play the predominant role. In both cases, path attenuation is fairly well estimated by ground-based radiometric data in terms of both FMR and FVR, while surface rain-rate retrieval show a lower FVR together with FMR slightly different from 1. Indeed, the FS1 frequency set, which is the one available at the considered ITALSAT ground station, results to be best suited for Cb observations. An optimum compromise might be to choose the frequency set FS3, i.e., 13.0, 31.7 and 50.0, which shows good performances in both Ns and Cb cases.

The second question, raised in point 2), is about the appropriateness of a cubic regression estimator. Incidentally, we have tested a cubic form similar to (13)–(15), but with mixed terms as well. Numerical results have yielded no significant improvements in terms of FMR and FVR with respect to (13)–(15). For a further comparison, we have considered a quadratic polynomial to represent (10) and (11), that is dropping the third power of T_Bs within (13)–(15). By using the FS1 frequency set for example, Table I illustrates the results of the inter-comparison between a quadratic and a cubic regression estimation in terms of FMR and FVR for surface rain-rate, columnar EWCs and path attenuations for a merged Ns–Cb data set. The quadratic form of regression estimators denotes slight differences in terms of FMR with respect to the cubic one, but yields in all cases a worsening of FVR scores. This is the reason why we have chosen the cubic form in the rest of the work. It is worth mentioning that, from Fig. 2, columnar ice contents are expected to be estimated with less accuracy than liquid water ones. In fact, in case of stratiform rainfall FVR values are 0.81, 0.98, 0.36 and 0.47 for C_c, C_r, C_g, and C_s, respectively, while in case of convective precipitation they are 0.76, 0.96, 0.84, and 0.73, respectively.

A third question regards the usefulness of a constrained regression with respect to the standard one, that is the applicability of (11) with respect to (10). In order to prove the choice in a quantitative way, we have performed some test case studies by arbitrarily altering the test noise bias and variance. The justification of these types of test resides in the fact that, as mentioned in Section III-A, noise sources in our inversion approach can be related to instrument, to measurement set up and to model assumptions. When considering all noise sources together and even disregarding radiometer calibration issues, error bias and deviation can be higher than 20 K.

Two test cases have been considered as extreme scenarios by increasing the mean value and standard deviation of the test additive noise by 10 K (Test 1) and 20 K (Test 2). By using a cubic estimator with FS1 frequency set and a merged Ns–Cb

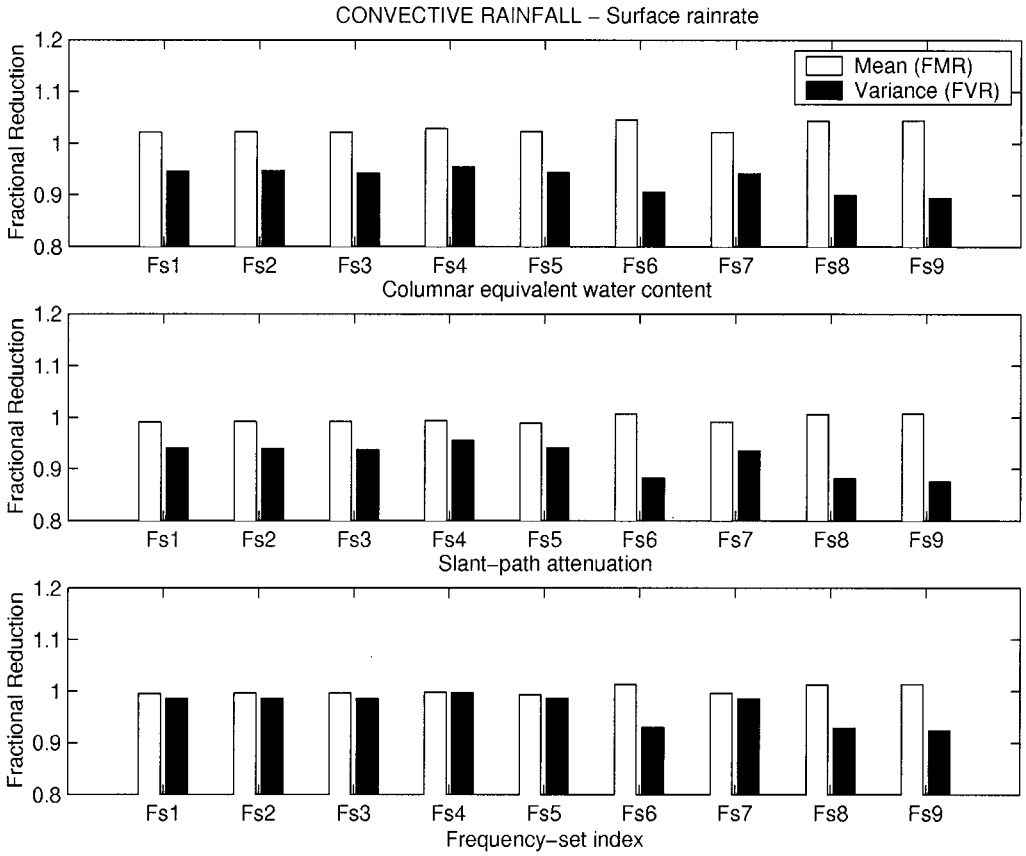

Fig. 7. The same as in Fig. 6, but for a convective rainfall.

TABLE I
COMPARISON BETWEEN QUADRATIC AND CUBIC OMR ALGORITHMS IN TERMS OF FMR AND FVR FOR RAIN-RATE, COLUMNAR EQUIVALENT WATER CONTENT (CEWCs), AND PATH ATTENUATION RETRIEVALS. PREDICTOR VECTOR CONSISTS OF 13.0-, 23.8-, AND 31.7-GHz T_Bs AT 41.8° ELEVATION ANGLE

	FMR		FVR	
	Quadratic	**Cubic**	**Quadratic**	**Cubic**
Surface rain-rate	1.0319	1.0220	0.9308	0.9439
Columnar EWC	0.9983	0.9904	0.9270	0.9399
Path attenuation	1.0022	0.9948	0.9754	0.9855

TABLE II
COMPARISON BETWEEN CUBIC OMR AND VMR RETRIEVAL ALGORITHMS IN TERMS OF FMR AND FVR FOR RAIN-RATE, CEWCs, AND PATH ATTENUATION RETRIEVALS FOR TWO TEST CASES. THE LATTER CONSIST IN ARBITRARILY INCREASING BOTH MEAN VALUE AND STANDARD DEVIATION OF TEST ADDITIVE NOISE OF 10 K (TEST 1) AND 20 K (TEST 2). CONSIDERED PREDICTOR VECTOR ARE 13.0-, 23.8-, AND 31.7-GHz T_Bs AT 41.8° ELEVATION ANGLE

	FMR				FVR			
	Test 1		Test 2		Test 1		Test 2	
	OMR	**VMR**	**OMR**	**VMR**	**OMR**	**VMR**	**OMR**	**VMR**
Surface rain-rate	1.6252	1.1464	0.4970	0.8368	2.1097	1.2655	-1.6079	0.8320
Columnar EWC	1.2229	1.0927	0.5936	0.7765	1.5386	1.1870	-0.7329	0.7637
Path attenuation	1.2270	1.1011	0.9208	0.9626	1.5051	1.2092	0.6613	0.8428

data set, Table II lists the results in terms of FMR and FVR by comparing ordinary and variance-constrained multiple regression for R, CEWC and A. Values of the constraint factor γ between 0.5 and 1.5 have been derived from (12) in these tests. The advantage of VMR against OMR in terms of robustness to noise and inversion stability is apparent especially when stressing test noise conditions as in Test 2. Notice that all previous test results, obtained by using OMR, are not substantially modified when carried out adopting VMR.

The final question is relative to the possibility to automatically discriminate between stratiform and convective clouds [28]. Numerical tests, using the same synthetic data mentioned so far, indicate that the estimation accuracy can benefit from this classification, especially when dealing with moderate rainfall. This impact can be also appreciated in a qualitative way by looking at Figs. 2–5 where the dynamic range of Ns simulations is much less than Cb ones. This aspect suggests that a polynomial regression derived from Cb training set could not

TABLE III
MEAN VECTOR $\mathbf{m}_{tk}$, INVERSE COVARIANCE MATRIX $\mathbf{S}_{tk}^{-1}$ AND THE DETERMINANT OF $\mathbf{S}_{tk}$ OF BRIGHTNESS TEMPERATURE AT 13.0, 23.8, AND 31.7 GHz FOR CLASSIFYING STRATIFORM AND CONVECTIVE RAIN USING A MAP TECHNIQUE. PREDICTOR VECTOR CONSISTS OF 13.0-, 23.8-, AND 31.7-GHz T_Bs AT 41.8° ELEVATION ANGLE

Stratiform Rainfall	**T_B at 13 GHz**	**T_B at 23.8 GHz**	**T_B at 31.7 GHz**
Mean $\boldsymbol{m}_{tk}$	16.2940	75.3914	63.5871
Inverse	0.3468	-0.1604	0.0124
auto-covariance	-0.1604	0.1687	-0.0622
$\boldsymbol{S}_{tk}^{-1}$	0.0124	-0.0622	0.0347
Ln(det($\boldsymbol{S}_{tk}$))	10.9715		

Convective Rainfall	**T_B at 13 GHz**	**T_B at 23.8 GHz**	**T_B at 31.7 GHz**
Mean $\boldsymbol{m}_{tk}$	78.7949	138.0690	134.3786
Inverse	0.0076	-0.0220	0.0129
auto-covariance	-0.0220	0.0715	-0.0442
$\boldsymbol{S}_{tk}^{-1}$	0.0129	-0.0442	0.0279
Ln(det($\boldsymbol{S}_{tk}$))	19.1352		

be the best fitting of moderate values of simulations due to Ns cloud structures.

Maximum *a posteriori* probability (MAP) criterion can be used to carry out cloud classification in a supervised context [9], [10]. If k is the rainfall class, i.e., Ns or Cb, then the conditional probability density function (PDF) of considered class k given a measurement $\mathbf{t}_m$ can be expressed as

$$p(k|\mathbf{t}_m) = \frac{p(\mathbf{t}_m|k)p(k)}{p(\mathbf{t}_m)} = \frac{p(\mathbf{t}_{mck})p(k)}{p(\mathbf{t}_m)} \tag{19}$$

where $\mathbf{t}_{mck} = \mathbf{t}_m - \mathbf{m}_{tk}$ is the perturbation of measurements from the mean value vector $\mathbf{m}_{tk}$ of class k and $p(k)$ represents the *a priori* discrete PDF of class k. Note that the expression of $\mathbf{t}_{mck}$ is similar to $\mathbf{t}_{mc}$, given in (9), except that the difference is made with respect to each rainfall class mean.

The MAP estimation of rainfall class k corresponds to the following maximization with respect k:

$$\hat{k} = \text{Mode}[\ln p(k|\mathbf{t}_m)] \tag{20}$$

where Mode is the PDF modal-value operator. If $p(\mathbf{t}_{mck})$ is assumed to be a multivariate Gaussian PDF, then (20) reduces to

$$\hat{k} = \text{Mode}[-(\mathbf{t}_m - \mathbf{m}_{tk})^T \mathbf{S}_{tk}^{-1}(\mathbf{t}_m - \mathbf{m}_{tk}) - N\ln(2\pi) - \ln(\det \mathbf{S}_{tk}) + 2\ln p(k)] \tag{21}$$

where $\mathbf{S}_{tk}$ is the T_B measurement auto-covariance matrix of class k and det is the matrix determinant.

Maximizing (21) means to know the radiometric mean $\mathbf{m}_{tk}$ and auto-covariance $\mathbf{S}_{tk}$ of each rainfall class k, that is Ns and Cb. This statistical characterization of each cloud class can be derived from the generated synthetic data set, while the prior PDF $p(k)$ can be used to subjectively weight each class as a function of other available information. Of course, mean vector $\mathbf{m}_{tk}$ and auto-covariance $\mathbf{S}_{tk}$ should be climatologically tuned in order to be, at least, representative of a given region during a specific season. Examples of $\mathbf{m}_{tk}$ and $\mathbf{S}_{tk}$ will be given in the next section.

If rainfall cloud classification is performed, the inversion scheme can be thought as two steps in cascade. That is, after discriminating between Ns and Cb, a polynomial regression algorithm, given by (13)–(15), can be applied using, as a training set, the data belonging to the selected rainfall class. This procedure implies that regression coefficients must be computed for each rainfall class.

IV. EXPERIMENTAL TESTS

Rainfall and path attenuation data acquired at the ground-station of ITALSAT geo-stationary satellite [11], located in Pomezia (Rome, Italy), have been used to test the model-based retrieval algorithms illustrated in the previous sections.

Since April 1994, measurements of the three ITALSAT-F1 propagation beacons at 18.7, 39.6, and 49.5 GHz are performed every second at an elevation angle of 41.8 degrees with a receiver-antenna of 3.5 m. The corresponding 3-dB beamwidths go from about 0.26° at 18.7 GHz to 0.12° at 39.6 GHz and 0.10° at 49.5 GHz. The ground station measures the amplitude and phase of co-polar and cross-polar signals of pencil beams at 18.7 and 39.6 GHz and the polarization transfer matrix at 49.5 GHz [35].

Concurrent measurements performed by two microwave radiometers (REC-1 and REC-2) pointed to the ITALSAT satellite, and a set of surface meteorological instruments including also a tipping-bucket rain gauge, are synchronously logged every 4 s by the ITALSAT ground-station [8]. The radiometric data are routinely used to assess the clear-air atmospheric reference level for calibrating the ITALSAT beacon clear-air path attenuation [12]. Radiosounding profiles are also available by the Italian Air-Force at least twice a day with the balloons launched at Pratica di Mare (Rome, Italy), about 5 km far from the ITALSAT ground-station.

In order to discriminate between stratiform and convective rainfall using (21), the radiometric mean $\mathbf{m}_{tk}$ and covariance $\mathbf{S}_{tk}$ (with its determinant) are needed for each class. By using available radiometric channels at 13.0, 23.8, and 31.7 GHz pointing at 41.8° elevation angle, Table III furnishes $\mathbf{m}_{tk}$, $\mathbf{S}_{tk}$ and $\det(\mathbf{S}_{tk})$ for Ns–Cb classification for a typical mid-season continental temperate climate, meteorologically characterized by radiosounding data acquired at Pratica di Mare. These table values will be used in the considered case studies.

TABLE IV
MAIN SPECIFICATIONS OF SINGLE-CHANNEL REC-1 RADIOMETER AT 13.0 GHz AND DUAL CHANNEL REC-2 RADIOMETER AT 23.8 AND 31.7 GHz, INSTALLED IN POMEZIA (ROME, ITALY) AT THE ITALSAT GROUND-STATION

Specifications	Values	*Specifications*	Values
Operating frequencies	REC-1: 13.0 GHz REC-2: 23.8, 31.7 GHz	*Azimuth axis rotation*	0° to 360°
Radiometric range	3 to 313 K	*Rate of rotation*	3°/sec.
Integration time ΔT	1, 2, 4, 8, 16, 32 sec.	*Pointing accuracy*	0.5 °
Radiometric resolution at ΔT=1 sec.	0.3 K	*Dimensions*	REC-1: 100x100x150 REC-2: 100x65x100 cm
Radiometric accuracy	1 K	*Weight*	REC-1: 220 kg REC-2: 200 kg
Dual-side bandwidth	400 MHz	*Power requirements*	220 VAC, 50 to 60 Hz
3-dB antenna beam-widths	3.5° at 13.0 GHz 1.9° at 23.8 GHz 1.8° at 31.7 GHz	*Output*	RS-232
Elevation axis rotation	-90° to +90°	*Control system*	Personal computer

A. Multifrequency Radiometric System

The REC-2 radiometer is a dual-channel system at 23.8 and 31.7 GHz, manufactured by the RESCOM company (Aalorg, Denmark). This radiometer is a compact self-contained configuration designed for automatic unattended operation for extended time with a high measuring accuracy. The REC-1 single channel radiometer is an independent system designed also by the RESCOM. The operating frequency is 13.0 GHz and, basically, it has the same mechanical characteristics of REC-2. The radiometers have an elevation and azimuth control and are controlled by a personal computer through an RS-232 serial line. Regular calibration are performed by using the tipping-curve method [25]. The main technical characteristics of the multi-frequency radiometric system are summarized in Table IV.

The REC-1 and REC-2 radiometers consist of offset-fed antenna parabolic reflectors connected to microwave receivers of the noise balancing type. The noise-balancing type receiver yields a high insensitivity to gain variations and mismatches within the noise injection feedback loop thus ensuring a high long-term stability. The actual temperatures of main microwave components in the front ends and feed assembly are monitored and used for correction of measured data. The antenna reflector and receiver sections are integrated in an outdoor box.

The shape of the antenna surfaces and the configuration of the wide-band feed horns have been designed so that energy outside the main lobes is minimized. Moreover, the extremely low side-lobes can ensure a minimum pick-up of radiation emitted from surrounding surface. By a proper design of the feed horn, nearly equal antenna main-lobes at 20 and 30 GHz have been obtained. The REC-2 corrugated feed horns is protected by an aperture window and is connected to a diplexer by a short waveguide bend. The REC-1 and REC-2 circular horns are horizontally polarized and placed above the antenna reflectors downward so that to be protected against rain drops, snow and condensation layer.

The REC-1 and REC-2 antenna reflectors are of carbon-fiber skin-honeycomb construction. They have a very smooth surface with roughness less than 0.2 mm. Their rectangular contour provides a projected aperture of about 90×90 cm^2 for REC-1 and 60×60 cm^2 for REC-2. Heated air is continuously blown across the antenna reflector which presents a set of small holes within its vertex area, thus preventing the formation of the dew and the possible accumulation of rain drops, snow and hail on the surface. Moreover, air from heater box is directed through a tube to the feed horn window. In this way, the window is kept free from condensation or rain drops.

The last features are essential when trying to use ground-based radiometry for rainfall remote sensing. As already discussed, the effect of water layers on the antenna reflectors can cause significant artifacts in the measured brightness temperatures. Unfortunately few studies on this subject are available in literature.

Jacobson *et al.* [16] carried out experimental and theoretical investigations for wetted flat reflectors at 20.6 and 31.7 GHz, inclined at 45° elevation. Theoretical results refer to a uniform plane wave obliquely incident upon a homogeneous water layer placed at the interface with a perfect conductor. Their analysis has showed that i) effects on measured T_B are polarization dependent with vertical-polarization impact higher than the horizontal polarization one up to 50%; ii) water layers of about 0.45 mm cause a maximum in both polarizations and frequencies with an increase of more than 500% with respect to clear-air measured T_B without water-layer effects; iii) water layers less than 0.2 mm can cause an increase of measured T_B less than 50%; iv) effects on measured T_B are azimuth-pointing dependent with a periodicity of about 90°.

Using a similar water layer model, Blevis [15] derived similar results for transmission and reflection loss at normal incidence. Consistently with transmission line theory, maximum reflection loss occurred for water layer thickness $d_w = \lambda_d/4$ with λ_d the plane-wave wavelength in the water-layer medium.

A very critical issue is the relationship between water-layer thickness and rainfall rate. Blevis used a formula initially derived for spherical radome surfaces in order to provide an approximation for parabolic reflectors [15]. Indeed, water layer thickness on paraboloids are not uniform and depend on antenna elevation being much less than those predicted for off-zenith angles. If the water-layer thickness is d_w [mm], then it can be related to antenna diameter D_A [cm] and to rainfall rate R [mm/h] by [15]

$$d_w^3 = 4.3011\ 10^{-10}\ D_A R. \tag{22}$$

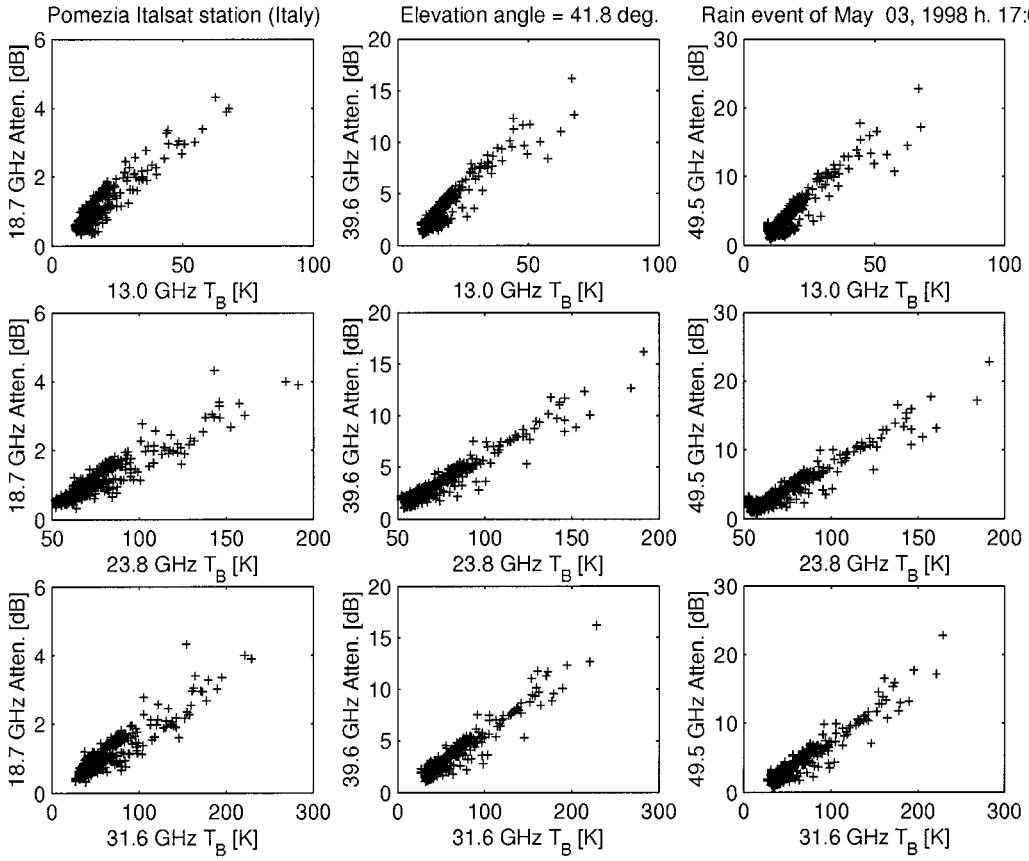

Fig. 8. For the case study of May 3, 1998, measured path attenuations at 18.7 GHz (left panels), 39.6 GHz (central panels), and 49.5 GHz (right panels) as a function of REC-1 and REC-2 radiometric measurements at 13.0 GHz (top panels), at 23.8 GHz (middle panels) and at 31.7 GHz (bottom panels). Graphic representation and observation parameters (frequency and pointing angle) are comparable to that of Figs. 4 and 5.

From (22), it turns out that for a reflector having $D_A = 60$ cm (e.g., REC-2 antenna), d_w is equal to 0.06 mm and 0.14 mm for R equal to 10 mm/h and 100 mm/h, respectively. For a reflector having $D_A = 90$ cm (e.g., REC-1 antenna), d_w is equal to 0.07 mm and 0.16 mm for $R = 10$ mm/h and $R = 100$ mm/h, respectively. Note that rain-rate R can be linked, in its turn, to water-flow rates F_w by means of $F_w = R/(A\rho_w)$ with A the antenna area and ρ_w the water density. For $R = 10$ mm/h and $R = 100$ mm/h, corresponding water flow rates are $F_w = 78$ ml/s and $F_w = 785$ ml/s for an antenna diameter of 60 cm and $F_w = 176$ ml/s and $F_w = 1767$ ml/s for an antenna diameter of 90 cm.

It is worth noting the water-layer thickness, predicted by (22), is always less than those measured by Jacobson *et al.* [16]. For water-flow rates of about 500 ml/s, (22) gives d_w less than 0.1 mm, while values from Jacobson *et al.* are of the order of 0.35 mm. This discrepancy can depend on the crude approximations behind (22) and on the difference between a plane and concave surface effects, but also on the difficulty to simulate realistic rainfall conditions even under a controlled experiment. For instance, rain water is generally not uniform over a surface and could be formed by small raindrops aggregation. Finally, it should be consider that the wet-reflector impact on measured antenna temperature in percentage decreases as the down-welling T_B increases: using (22) and $d_w = 0.1$ mm, it can go from an overestimation of about 70% for down-welling $T_B = 50$ K to about 10% for $T_B = 150$ K.

In order to test the efficiency of water-layer removal of the REC radiometric system, we have carried out some experimental tests [16], [36]. A fairly uniform water flux, with values going from 50 to 1500 ml/s, has been distributed over the REC-1 and REC-2 parabolic reflectors inclined at 41.8° elevation angle. The empirical evidence was that, thanks to the blower and to the reflector holes, the observed water layers on the antenna dish had a thickness less than 0.15 mm. These values are in a way consistent with those predicted by (22). A changing behavior has been noted as a function of the elevation angle, the zenith pointing being the worst condition as intuitive. From theoretical results, we should expect an impact on measured T_Bs less than 20% at 23.8 and than 50% at 31.6 GHz with respect to clear-air T_Bs not affected by water-layer emission [16]. These results corroborate the choice of a robust estimator, as VMR in (11), with respect to an ordinary one, as OMR in (10).

To further assess the impact of wetted reflectors on T_Bs, the adopted model-based approach can help to perform a preliminary data quality control as well. The idea is to use modeled T_Bs, simulated from synthetic rainfall clouds, to verify whether measured T_Bs in rainy conditions belong or not to the simulation domain. This approach is conditioned, of course, to the representativeness of rainfall radiative models with respect to measurement site and period. The latter task might be done using other available information derived from coincident beacon path attenuation, meteorological measurements and rain gauge data.

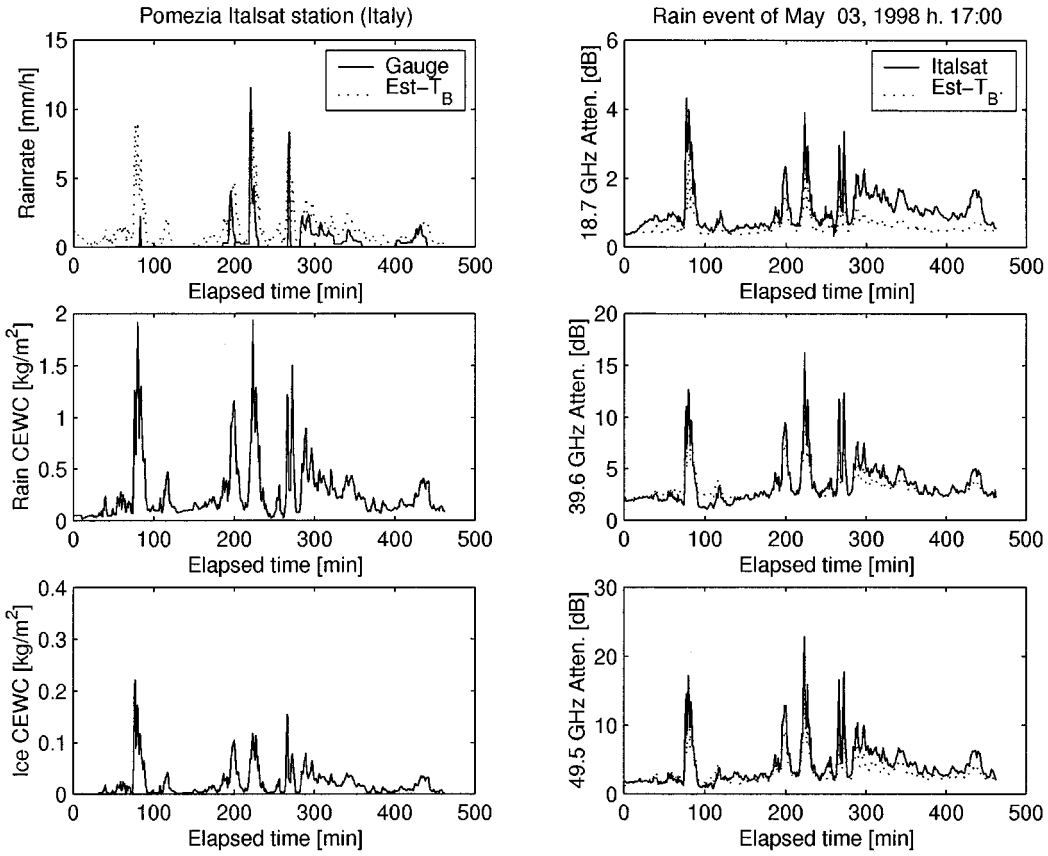

Fig. 9. For the case study of May 3, 1998, estimated rainfall rate, columnar EWC of rain and columnar EWC of ice (left panels) and estimated path attenuation at 18.7 GHz, 39.6 GHz and 49.5 GHz (right panels) as compared to available rain gauge data and corresponding measured ITALSAT path attenuations, both indicated by solid lines. Retrieval algorithm is cubic variance-constrained multiple regression (VMR) applied to REC-1 and REC-2 radiometric measurements at 13.0 GHz, at 23.8 GHz and at 31.7 GHz.

The way to proceed is very similar that used to assess clear-air and cloudy radiometric data in order to eliminate possible data outliers [3], [5]. An application of this concept will be illustrated in Section IV-C.

B. Case Study of Moderate Rainfall

In order to show an example, we have selected a case of light to moderate rainfall, observed in Pomezia during May 3, 1998. A moving average with 1-minute window and 1-minute sampling period has been applied to analyze all raw data. As a rainfall retrieval algorithm, VMR has been chosen in all tests.

Fig. 8 shows the measured path attenuation for the ITALSAT channel frequencies at 18.7, 39.6 and 49.5 GHz as a function of the down-welling brightness temperatures at 13.0, 23.8, and 31.7 GHz, both for a 41.8° elevation angle. These results can be compared with those of Fig. 4 in order to verify the consistency between simulation and measurements. Less dispersion and a slight tendency of simulated data to underestimate measured values is noted, especially at low frequencies. The reason of this discrepancy might be searched either in a light-rainfall modeling inadequacy or in the additional emission due thin water-layer film on the reflectors.

By applying the MAP classification and even from a qualitative evaluation, the discrimination is clearly toward a stratiform rainfall case. This is in a way confirmed by looking at path attenuation measurements which are less than 5 dB and 25 dB at 18.7 GHz and 49.5 GHz, respectively. Notice that a careful selection of a rainfall subsample of measured data should be performed in order to apply the retrieval to the measured data in excess with respect to clear-air values. This can be done by referring to measured path attenuation and T_B reference values in clear-air conditions.

The top-left panel of Fig. 9 shows the time-series of the rainfall rate estimate from the three-channel radiometer as compared to the rain-gauge measurements. The panels just below show the columnar rain and ice content estimates. The right panels show the time series of slant-path attenuation estimates as compared to the corresponding ITALSAT measurements at 18.7, 39.6, and 49.5 GHz.

The rms error between estimated and measured rain rate is about 1.4 mm/h, while for path attenuation rms error is 0.52, 0.86, and 1.57 dB at 18.7, 39.6, and 49.5 GHz, respectively. As said, rain rate is measured at a given point by a rain-gauge and along the link path by microwave radiometers, while the comparison in terms of measured and estimated attenuation is between fairly homogeneous data. If other channel combinations are used, e.g., only 23.8 and 31.7 GHz, no significant variation of the obtained rms errors is noted.

C. Case Study of Intense Rainfall

A case study of intense rainfall observed in Pomezia during August 28, 1998, has been analyzed with the same data preprocessing as above.

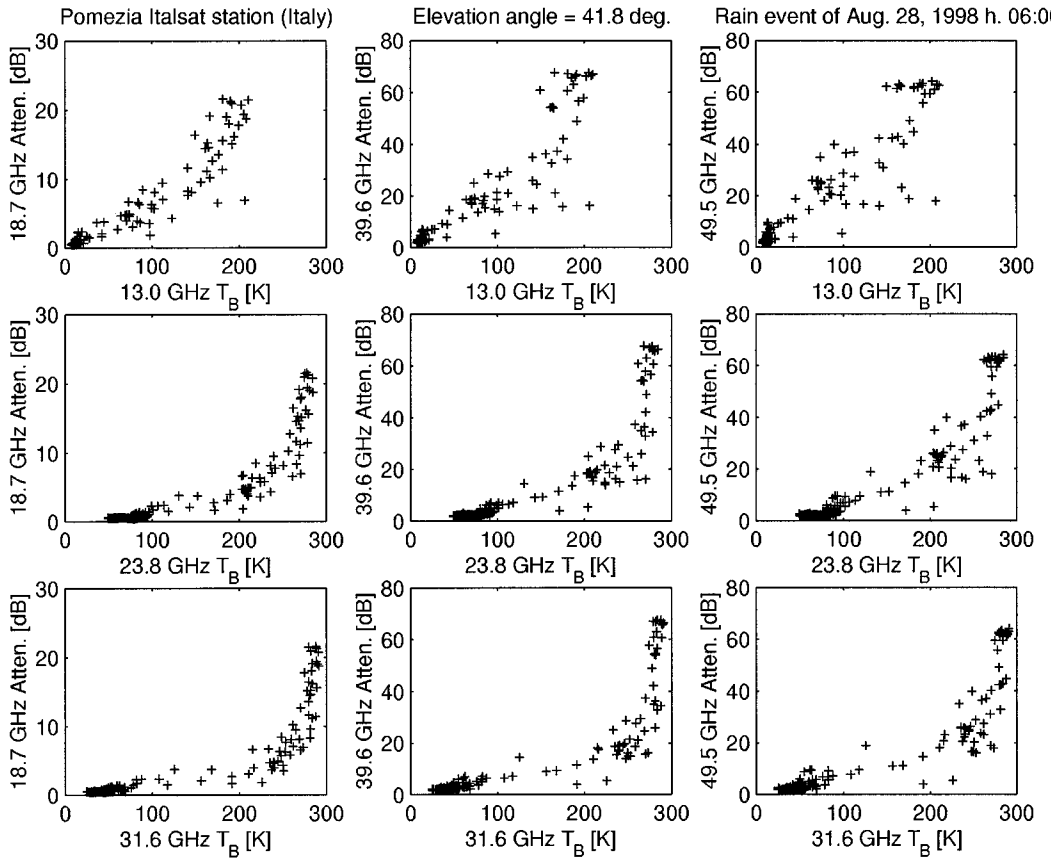

Fig. 10. The same as in Fig. 8, but for the case study of August 28, 1998.

Similarly to Fig. 8, Fig. 10 shows the measured path attenuation for the ITALSAT channel frequencies at 18.7, 39.6, and 49.5 GHz as a function of down-welling T_Bs at 13.0, 23.8, and 31.7 GHz, both for a 41.8° elevation angle. Again, these results can be compared with those of Fig. 5 in order to verify the agreement between simulation and measurements. The agreement is fairly satisfying at 23.8 and 31.7 GHz, while denoting a measured-T_B saturation effect at 13.0 GHz around 200 K. An explanation of the latter behavior is due to the larger beam-width of 13.0-GHz channels which could cause a high variability of atmospheric state within the beam. The discrepancy between measurements and simulations could be read either as a symptom of incomplete representativeness of the adopted cloud radiative model with respect to measured radiometric data or, vice versa, as an inadequateness of the latter to fulfill forward modeling assumptions. We will come back to this point later on.

In this case study, by applying the MAP classification, the decision is now toward a convective rainfall. Path attenuation measurements up 50 dB at 49.5 GHz corroborate this automatic discrimination.

The left panels of Fig. 11 shows the time-series of the rainfall rate estimate from the three-channel radiometer together with the columnar rain and ice content estimates. The comparison with rain-gauge measurements has been not possible due to the lack of rain-gauge data during the event. The right panels show the time series of the path-attenuation estimates as compared to the corresponding ITALSAT measurements at 18.7, 39.6, and 49.5 GHz.

The rms differences between estimated and measured path attenuation at 18.7, 39.6, and 49.5 GHz are 1.81, 7.74, and 6.45 dB, respectively. Even though comparisons in terms of measured and estimated attenuation is between consistent path-integrated data, discrepancies in the attenuation comparison can arise from the difference between the ITALSAT and radiometer antenna beam-widths (see Section IV-A and Table IV), the latter being even 10 times greater than ITALSAT ones. When observing a small convective rain cell along the slant path, nonhomogeneous beam filling can significantly affect radiometric measurements, especially at 13.0 GHz, as suggested by Fig. 10 [13], [14]. This might explain the evident underestimation of path attenuation between minutes 170 and 200 when using all three radiometric channels applied to a plane-parallel cloud radiative training model, described in Section II.

To indirectly prove the latter explanation, we have performed a simple test consisting in dropping T_B measurements at 13.0 GHz from the predictor vector $\mathbf{t}_m$ in (11) and rely only on 23.8 and 31.7 GHz T_Bs having relatively small beam-widths (and thus less affected by nonuniform beam filling). The resulting estimates are shown in Fig. 11 by the dashed thick line which does not exhibit the already mentioned saturation and is able to partially follow ITALSAT attenuation peaks within the convective period around minute 200. The rms errors reduces to 1.56, 6.69 and 6.02 dB at 18.7, 39.6, and 49.5 GHz, respectively. The latter results comply well with quantitative evaluation of radiometric beam-filling effects in case of intense rainfall of limited extent. In particular, in these circumstances Brussaard suggests

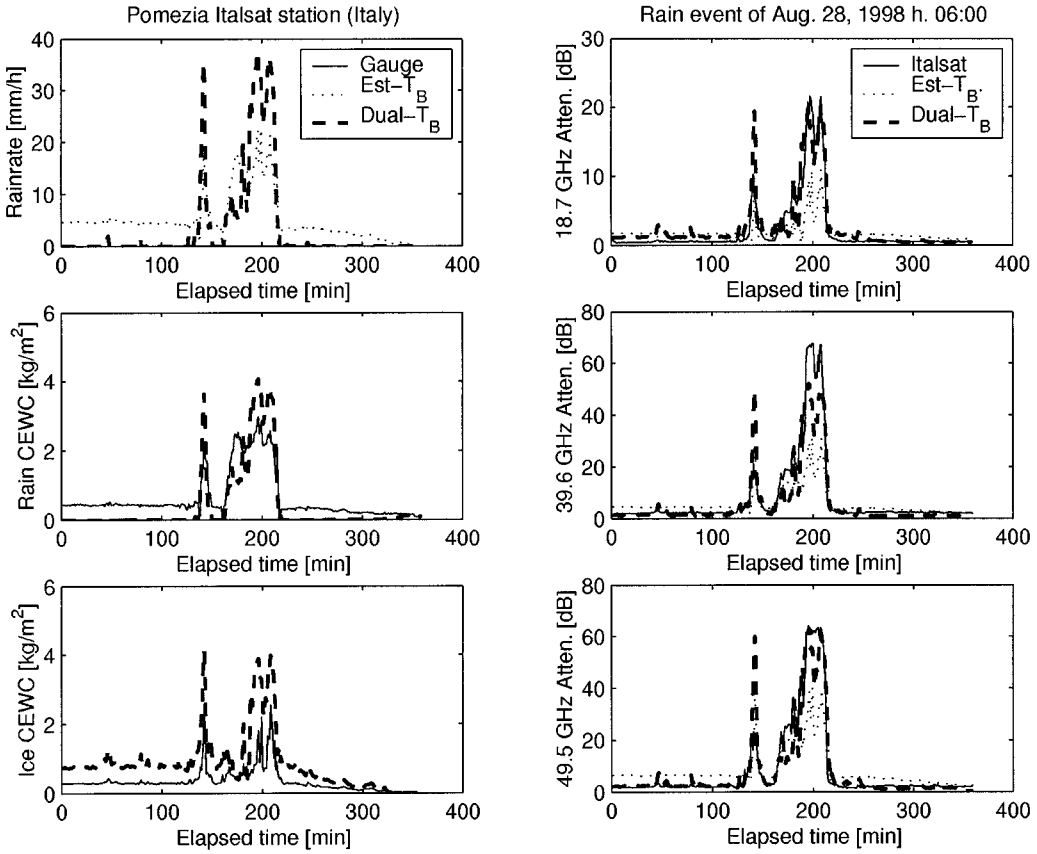

Fig. 11. The same as in Fig. 9, but for the case study of August 28, 1998. Rain gauge data were not available during this event. Thick dashed lines refer to path attenuation estimates carried out by using only REC-2 radiometric measurements at 23.8 GHz and at 31.7 GHz.

an underestimation of T_B of at least 5% (with an antenna pattern efficiency of 0.945 at 11.4 GHz) [13].

V. Conclusion

Statistical inversion algorithms for ground-based retrieval of surface rain-rate and integrated cloud parameters have been proposed and tested. The retrieval methods have been trained by numerical simulations of a radiative transfer model applied to microphysically-consistent precipitating cloud structures, discriminating between stratiform (Ns) and convective (Cb) rainfall clouds.

A variance-constrained regression technique has been developed and tested on synthetic data in order to understand its potentiality for robust estimation surface rain-rate, columnar hydrometeor contents and path attenuations. To select the optimal algorithm and frequency set for rainfall estimation, numerical tests have been carried out by comparing results in terms of fractional mean and variance reduction, i.e., FMR an FVR.

Cubic multiple regression performs quite well both for Ns and Cb cases, showing that the role of lower frequencies (below 20 GHz) is significant when trying to estimate cloud parameters of intense precipitation. Higher frequencies (above 40 GHz) can successfully help when observing stratiform rain clouds. Microwave frequencies around 30 GHz can be considered always useful due to their high sensitivity to cloud liquid. To this aim, a maximum *a posteriori* probability (MAP) classificator has been described to automatically discriminate between Ns and Cb in a cascade inversion scheme.

Ground-based radiometric measurements at 13.0, 23.8, and 31.7 GHz have been used for an experimental test of the retrieval algorithms. Comparison with rain-gauge data and rain path-attenuation measurements, derived from ITALSAT channels, have been performed for two selected cases of moderate and intense rainfall. A fairly good agreement between estimates and measurements has been achieved. In contrast with numerical results on synthetic horizontally-stratified cloud structures, the experimental test has emphasized the possible effects of nonhomogeneous radiometric beam filling when looking at horizontally-finite small rain cells, especially at low frequencies such as 13.0 GHz. It has been shown that the this beam effect on measured T_Bs reflects into an underestimate of rainfall slant-path attenuation when using a plane-parallel cloud radiative training model. Finally, the remarkable result obtained in this work is the ability to follow path attenuation dynamics over relatively long periods by using a robust estimator applied to radiometric microwave measurements both in stratiform and convective rainfall.

Appendix

The variance-constrained multiple regression (VMR), given in (11), can be seen as a further special case within the theoretical framework illustrated by Crone *et al.* [33]. The derivation of VMR is very similar to what they called *ridge* regression.

As already mentioned in the main text, we will denote vectors and matrices by bold lowercase and uppercase symbols, respectively. Scalars will be indicated by italic letters.

Let $\mathbf{X}_c$ be the $M \times L$ matrix containing L observations of M centered parameters (or *predictands*, given by $\mathbf{x}_c$ for each realization) and $\mathbf{T}_{mc}$ be the $N \times L$ matrix containing L observations of N centered measurements (or *predictors*, given by $\mathbf{t}_{mc}$ for each realization). The auto- and cross-covariance matrices, appearing in (10) and associated with this sample, can be optimally estimated by means of

$$\mathbf{S}_t = \frac{1}{L-1}\,\mathbf{T}_{mc}\mathbf{T}_{mc}^T \tag{A1}$$

and

$$\mathbf{S}_{xt} = \frac{1}{L-1}\,\mathbf{X}_c\mathbf{T}_{mc}^T. \tag{A2}$$

In order to derive (11), it is useful to introduce the sum of squared errors (E^2) of estimate through the following expression:

$$E^2 = \mathrm{Tr}[(\mathbf{X}_c - \mathbf{D}\mathbf{T}_{mc})(\mathbf{X}_c - \mathbf{D}\mathbf{T}_{mc})^T] \tag{A3}$$

where $\mathbf{D}$ is the unknown $M \times N$ regression matrix. The VMR solution matrix, i.e., $\mathbf{D}_{\mathrm{VMR}}$, is the $\mathbf{D}$ matrix which satisfies the following minimization:

$$\frac{\delta}{\delta D}\left[\mathrm{Tr}(\mathbf{D}_{\mathrm{VMR}}\mathbf{V}\mathbf{V}^T\mathbf{D}_{\mathrm{VMR}}^T) + \lambda E^2)\right] = 0 \tag{A4}$$

where λ is the Lagrange multiplier and the derivative is performed with respect to the elements of the matrix $\mathbf{D}$. The variance-constraining matrix $\mathbf{V}$ in (A4) is a $N \times L$ matrix whose auto-covariance $\mathbf{S}_v$ is given by

$$\begin{aligned}\mathbf{S}_v &= \frac{1}{L-1}\,\mathbf{V}\mathbf{V}^T = \frac{1}{L-1}\,diag[diag(\mathbf{T}_{mc}\mathbf{T}_{mc}^T)] \\ &= diag[diag(\mathbf{S}_t)].\end{aligned} \tag{A5}$$

From (A5), the elements of the main diagonal of $\mathbf{S}_v$ are equal to the corresponding ones of $\mathbf{S}_t$, being zero all other extra-diagonal components [see the definition of $diag$ in (18)]. Equation (A4) corresponds to minimize the given matrix trace subject to the constraint to keep E^2 constant.

From (A4), it can be derived the following expression:

$$2\mathbf{D}_{\mathrm{VMR}}\mathbf{V}\mathbf{V}^T + \lambda(-2\mathbf{X}_c\mathbf{T}_{mc}^T + 2\mathbf{D}_{\mathrm{VMR}}\mathbf{T}_{mc}\mathbf{T}_{mc}^T) = 0, \tag{A6}$$

that is, using (A1), (A2), and (A5)

$$\frac{1}{\lambda}\,\mathbf{D}_{\mathrm{VMR}}\mathbf{S}_v + \mathbf{D}_{\mathrm{VMR}}\mathbf{S}_t = \mathbf{S}_{xt}. \tag{A7}$$

Finally, by setting the multiplier $\lambda = 1/\gamma$, from (A7) we have

$$\mathbf{D}_{\mathrm{VMR}} = \mathbf{S}_{xt}(\mathbf{S}_t + \gamma\mathbf{S}_v)^{-1} \tag{A8}$$

whose form explains the expression of the third member of (11). If the *constraint factor* γ is equal to zero, then (A8) reduces to the OMR given by (10).

ACKNOWLEDGMENT

The authors are grateful to Dr. M. D. Jacobson for providing them with his unpublished report and for his helpful suggestions on wet reflectors' topic. Instrumentation maintenance and data acquisition were carefully carried out by F. Consalvi (FUB).

REFERENCES

[1] E. R. Westwater, "Ground-based microwave remote sensing of meteorological variables," in *Atmospheric Remote Sensing by Microwave Radiometry*, M. A. Janssen, Ed. New York: Wiley, 1993.

[2] E. R. Westwater and O. N. Strand, "Statistical information content of radiation measurements used in indirect sensing," *J. Atmos. Sci.*, vol. 25, pp. 750–758, 1968.

[3] E. R. Westwater, J. B. Snider, and M. J. Falls, "Ground-based radiometric observation of atmospheric emission and attenuation at 20.6, 31.75 and 90.0 GHz: A comparison of measurements and theory," *IEEE Trans. Antennas Propagat.*, vol. 38, pp. 1569–1580, 1990.

[4] C. Matzler, "Ground-based observations of atmospheric radiation at 5, 10, 21, 35, and 94 GHz," *Radio Sci.*, vol. 27, pp. 403–415, 1992.

[5] P. Ciotti, P. Basili, G. d'Auria, F. S. Marzano, and N. Pierdicca, "Microwave radiometry of the atmosphere: An experiment from a sea-based platform during ERS-1 altimeter calibration," *Int. J. Remote Sens.*, vol. 16, pp. 2341–2356, 1995.

[6] J. L. Vivekanandan and L. Li, "Microwave radiometric technique to retrieve vapor, liquid and ice—Part I: Development of a neural-network based inversion method," *IEEE Trans. Geosci. Remote Sensing*, vol. 35, pp. 224–236, 1997.

[7] B. E. Sheppard, "Effect of rain on ground-based microwave radiometric measurements in the 20–90 GHz," *J. Atmos. Oceanic Technol.*, vol. 13, pp. 1139–1151, 1996.

[8] F. S. Marzano, E. Fionda, P. Ciotti, and A. Martellucci, "Rainfall retrieval from ground-based multichannel microwave radiometers," in *Microwave Radiometry and Remote Sensing of the Environment*, P. Pampaloni, Ed. Utrecht, The Netherlands: VSP, 1999, ISBN 90-6764-318-4, pp. 397–405.

[9] N. Pierdicca, F. S. Marzano, G. d'Auria, P. Basili, P. Ciotti, and A. Mugnai, "Precipitation retrieval from spaceborne microwave radiometers based on maximum *a posteriori* probability estimation," *IEEE Trans. Geosci. Remote Sens.*, vol. 34, pp. 831–846, 1996.

[10] F. S. Marzano, A. Mugnai, G. Panegrossi, N. Pierdicca, E. A. Smith, and J. Turk, "Bayesian estimation of precipitating cloud parameters from combined measurements of spaceborne microwave radiometer and radar," *IEEE Trans. Geosci. Remote Sensing*, vol. 37, pp. 596–613, 1999.

[11] B. R. Arbesser-Rastburg and A. Paraboni, "European research on Ka-band slant path propagation," *Proc. IEEE*, vol. 85, pp. 843–852, 1997.

[12] F. S. Marzano and C. Riva, "Evidence of long-term correlation between clear-air scintillation and attenuation in microwave and millimeter-wave satellite links," *IEEE Trans. Antennas Propagat.*, vol. 47, pp. 1749–1757, 1999.

[13] G. Brussaard, "Radiometry. A useful prediction tool?," European Space Agency Report SP-1071, Nordwijk, The Netherlands, 1985.

[14] F. S. Marzano, E. Fionda, and P. Ciotti, "Simulation of radiometric and attenuation measurements along earth-satellite links in the 10- to 50-GHz band through horizontally-finite convective raincells," *Radio Sci.*, vol. 34, pp. 841–858, 1999.

[15] B. C. Blevis, "Losses due to rain on radomes and antenna reflecting surfaces," *IEEE Trans. Antennas Propagat.*, vol. 14, pp. 175–176, 1966.

[16] M. D. Jacobson, D. C. Hogg, and J. B. Snider, "Wet reflectors in millimeter-wave radiometry—Experiment and theory," *IEEE Trans. Geosci. Remote Sensing*, vol. GE-24, pp. 784–791, 1986.

[17] M. D. Jacobson, "Design and performance of a spinning flat reflector for millimeter-wave radiometry," *IEEE Trans. Geosci. Remote Sensing*, vol. 35, pp. 464–466, 1997.

[18] G. d'Auria, F. S. Marzano, N. Pierdicca, R. Pinna Nossai, P. Basili, and P. Ciotti, "Remotely sensing cloud properties from microwave radiometric observations by using a modeled cloud data base," *Radio Sci.*, vol. 33, pp. 369–392, 1998.

[19] D. C. Hogg, "Rain, radiometry, and radar," *IEEE Trans. Geosci. Remote Sensing*, vol. 27, pp. 576–585, 1989.

[20] Z. S. Haddad, S. L. Durden, and E. Im, "Stochastic filtering of rain profiles using radar, surface-referenced radar, or combined radar-radiometer measurements," *J. Appl. Meteorol.*, vol. 35, pp. 229–242, 1996.

[21] K. N. Liou, *An Introduction to Atmospheric Radiation*. New York: Academic, 1980.
[22] L. Tsang, J. A. Kong, and R. T. Shin, *Theory of Microwave Remote Sensing*. New York: Wiley, 1985.
[23] R. Wu and J. A. Weinman, "Microwave radiances from precipitating clouds containing aspherical ice, combined phase, and liquid hydrometeors," *J. Geophys. Res.*, pp. 7170–7178, 1984.
[24] C. Matzler and A. Standley, "Relief effects for passive microwave remote sensing," *Int. J. Remote Sensing*, vol. 21, pp. 2403–2412, 2000.
[25] Y. Han and E. R. Westwater, "Analysis and improvement of tipping calibration for ground-based microwave radiometers," *IEEE Trans. Geosci. Remote Sensing*, vol. 38, pp. 1260–1276, 2000.
[26] K. Stamnes, S. Tsay, W. Wiscombe, and K. Jayaweera, "Numerically stable algorithm for discrete-ordinate-method radiative transfer in multiple scattering and emitting layered media," *Appl. Opt.*, vol. 27, pp. 2502–2509, 1988.
[27] R. A. Houze, "Structures of atmospheric precipitation systems: A global survey," *Radio Sci.*, vol. 17, pp. 671–689, 1982.
[28] Y. C. Hong, C. D. Kummerow, and W. S. Olson, "Separation of convective and stratiform precipitation using microwave brightness temperature," *J. Appl. Meteorol.*, vol. 38, pp. 1195–1213, 1999.
[29] F. S. Marzano and P. Bauer, "Sensitivity analysis of airborne microwave retrieval of stratiform precipitation to the melting layer parameterization," *IEEE Trans. Geosci. Remote Sensing*, vol. 39, pp. 75–91, Jan. 2001.
[30] H. Liebe, "An atmospheric millimeter-wave propagation model," *Int. J. Inf. Millim.-Waves*, vol. 10, pp. 367–378, 1989.
[31] H. Czekala and C. Simmer, "Microwave radiative transfer with nonspherical precipitating hydrometeors," *J. Quant. Spectrosc. Radiat. Transf.*, vol. 60, pp. 365–374, 1998.
[32] C. D. Rogers, "Retrieval of atmospheric temperature and composition from remote measurement of thermal radiation," *Rev. Geophys. Space Phys.*, vol. 14, pp. 609–624, 1976.
[33] L. J. Crone, L. M. McMillin, and D. S. Crosby, "Constrained regression in satellite meteorology," *J. Appl. Meteor.*, vol. 35, pp. 2023–2039, 1996.
[34] M. D. King, "Sensitivity of constrained linear inversions to the selection of Lagrange multiplier," *J. Atmos. Sci.*, vol. 39, pp. 1356–1369, 1982.
[35] A. Aresu, E. Damosso, A. Martellucci, L. Ordano, and A. Paraboni, "Depolarization of electromagnetic waves due to rain and ice: Theory and experimental results," *Alta Freq.*, vol. 6, pp. 70–75, 1994.
[36] M. D. Jacobson, private communication, 2000.

Frank Silvio Marzano (S'89–M'99) received the Laurea degree (cum laude) in electrical engineering and the Ph.D. degree in applied electromagnetics both from the University "La Sapienza" of Rome, Italy, in 1988 and 1993, respectively.

In 1993 he collaborated with the Institute of Atmospheric Physics, CNR, Rome, Italy. From 1994 until 1996, he was with the Italian Space Agency, Rome, Italy, as a Post-doctorate Researcher. After being a Lecturer at the University of Perugia, Italy, in 1997 he joined the Department of Electrical Engineering, University of L'Aquila, Italy, where he presently teaches a course on electromagnetic fields. His current research concerns passive and active remote sensing of the atmosphere from ground-based, airborne, and spaceborne platforms, with a particular focus on precipitation using microwave and infrared data, development of inversion methods, radiative transfer modeling of scattering media, and scintillation and rain-fading analysis along satellite microwave links.

Dr. Marzano received the Young Scientist Award of XXIV General Assembly of the International Union of Radio Science (URSI) in 1993. In 1998 he was the recipient of the Alan Berman Publication Award (ARPAD) from the Naval Research Laboratory, Washington, DC. Since 2001, he has been the national delegate for the European COST actions n. 280 and 720.

Ermanno Fionda received the degree in physics from the University of Roma "La Sapienza" in 1980.

From 1981 to 1982 he joined the Atmospheric Physics Institute (IFA-CNR, Roma) where he worked on the energetic balance in the lower atmospheric layer. Since 1983 he has been with the "Ugo Bordoni" Foundation, Rome. His major research experience has been on various influences of the Earth's atmosphere on radio waves for communication also including remote sensing techniques of troposphere properties. His particular areas of interest are scintillation, scattering and absorption–emission processes at frequencies from 10 to 50 GHz using satellite links and ground-based microwave radiometers. Presently he is involved in the studies of water vapor estimation using different techniques including GPS data.

Piero Ciotti (M'94) received the Laurea (Doctor's) degree in electronic engineering (cum laude) from the University of Rome, Italy, in 1977.

He joined the Department of Electronic Engineering, University "La Sapienza," Rome, in 1977 where he served first as an Assistant Professor and, since 1987, as a Associate Professor, teaching a course on remote sensing. In April 2000, he bacame Full Professor of electromagnetics at the same university. During 1984–1985, he conducted research at the NOAA/ERL Wave Propagation Laboratory, Boulder, CO, on a NATO/CNR fellowship. He was a member of the ESA Calibration Team for the ERS-1 Radar Altimeter and a Principal Investigator of the ESA/JRC MAESTRO airborne SAR campaign. He is also Principal Investigator of an ESA/ENVISAT accepted research proposal and member of RA-2/MWR, MERIS and SCIAMACHY Calibration Teams. Since 1991, he has been with the Department of Electrical Engineering, University of L'Aquila, L'Aquila, Italy, where he has taught courses on signal theory, electromagnetic fields, and electromagnetic wave propagation. His research activity has been concerned with radiometric remote sensing of the atmosphere, microwave line-of-sight propagation, inverse electromagnetic problems, and digital signal processing.

Antonio Martellucci was born in Rome, Italy, on April 10, 1963. He received the degree in electronic engineering and the Ph.D. degree in electromagnetic science in 1992.

After the degree he worked in Fondazione Ugo Bordoni (FUB), Rome, as a consultant on optical communication system. Then he joined ALENIA, in 1988, working on optical system for remote sensing. In 1988, he rejoined FUB, where he has been involved in propagation studies for spatial communication systems. He is currently a Staff Member in the electromagnetic division of the ESA/ESTEC (The Netherlands). His research activities concerned mainly the attenuation, depolarization, interference and sky noise due to rain, ice, atmospheric gases and clouds performing both theoretical and experimental analysis. He has been involved in Olympus and Italsat experimental activities as well as various ESA/ESTEC and INTELSAT research contracts and activities in addition to ITU-R and COST working groups. He is author of 13 books and transaction papers, 45 conference papers, and more than 20 internal, contract, and research reports.